The multi-phase baryon cycle in a local infrared-luminous galaxy merger

Eirik Elias Prydz Fredborg

Thesis submitted for the degree of
Master of Science in Astronomy

Institute of Theoretical Astrophysics
University of Oslo

16th of May, 2022

Abstract

AGN and stellar feedback play vital roles in the redistribution of gas in galaxies. Feedback can potentially affect the star formation rates and therefore the evolution of a galaxy. This thesis presents a spatially resolved analysis of the multi-phase outflow in a single local ultra luminous infrared galaxy (ULIRG). The work is presented as a possible building block for more detailed analyses of the connection between the feedback processes in galaxies with the goal of a better understanding of the processes driving galaxy evolution.

Observations performed by the Atacama Large Millimeter/Submillimeter Array (ALMA) and the Multi Unit Spectroscopic Explorer (MUSE) instrument of the Very Large Telescope (VLT) were used to study the local ULIRG, IRAS 20100 -4156. The molecular and ionised gas phases were studied, traced by the CO(1-0) and [OIII]5007 lines respectively.

The galaxy is found to have outflows extending out to ~ 5 and $\sim 7-8$kpc for the molecular and ionised gas phases respectively. The gas phases do not follow the same kinematics. The molecular phase is reported to have approximately constant velocity as a function of distance to the galactic centre. The ionised gas is characterised by a clear trend of decrease in velocity at greater distances from the galactic centre. It is hypothesised that the cause for this lack of similarity in kinematics is that stellar feedback is a significant contributor to the molecular outflow and not the ionised outflow. Clear signs of oppositely directed outflows are reported, indicating that these outflows are driven by relativistic jets ejected by the central AGN.

Peak outflow velocities for the molecular and ionized phases are ~ 1000 and ~ 1200km/s respectively. Spatially averaged velocities are determined to be 650 ± 60 and 776 ± 19km/s, consistent with previously published results on the source.

I have estimated the outflow mass rate only for the molecular gas phase, which is believed to carry most of the mass of galactic outflows in (U)LIRGs. The total outflow mass rate is estimated to be $\dot{M}_{outf}(H_2) = 1360 \pm 340 M_{\odot}\mathrm{yr}^{-1}$, also consistent with results in the literature. The spatially resolved analysis estimate the outflow mass rates to be over 6 times greater in the regions closest to the galactic centre, than any other region.

The methods of spatially resolved analysis show great potential, and would be beneficial to include in statistical analyses of samples of galaxies.

Acknowledgments

I would like to thank my thesis supervisor Claudia Cicone for her support, high expectations and all her constructive feedback. I also would like to thank my family, and especially my girlfriend, Helle, for their continuous support and patience for my excitement in my studies of gas in a galaxy far away. Lastly, I would like to thank my fellow master students at the institute for all our long lunches and healthy discussions.

Contents

List of Figures

Chapter 1

Introduction

1.1 Galaxy formation and evolution

The rate of which molecular gas collapses and form stars is one of the most fundamental observables when studying the evolution of galaxies. The star formation rate (SFR) is a direct measure of the rate of which baryonic structures form in the universe. Studies on the history of star formation rates (SFR) has shown that galaxies with SFRs of more than 100 $M_{\odot}$/yr were more abundant earlier when the universe was only 2-3 Gyr old (Barger et al. (1998), Daddi et al. (2005) and Gruppioni et al. (2013)). Figure 1.1 illustrates this history of SFR by plotting star formation rate density (SFRD) as a function of redshift. The figure shows that the star formation density peaks at $z \sim 2$ and then rapidly declines until $z = 0$.

Stars are made of collapsing molecular gas clouds and a galaxies ability to continuously form new stars is predicated on the availability of molecular gas. Galaxies at redshift $z > 1$ has been found to have gas depletion times of less than a Gyr (Daddi et al. (2010), Genzel et al. (2010) and Tacconi et al. (2013)), meaning that they would use up their molecular gas reservoir with their current SFR in less than 10^9 years. Without replenishment, stars would stop beeing formed, and as the existing stars burn out the galaxy would slowly die. The need for gas accretion into galaxies from the surrounding intergalactic medium (IGM) is evident from observations at all redshifts Putman (2017).

1.1.1 Galaxy mergers

Mergers between galaxies have long been thought to have an impact on the SFR, with observations of galaxy mergers showing reduced, enhanced and highly enhanced star formation (Pearson et al. (2019). Knapen et al. (2015), Silva et al. (2018) and Ellison et al. (2013) find that galaxy interactions increase the SFR, but only up to a factor of two, considering galaxies with redshift $z < 2.5$. The work of Pearson et al. (2019) considers samples of over 200 000 galaxies at redshift between 0 and 4 from the SDSS, KiDS and CANDELS imaging surveys. Their study determines if there is significant change in SFR in merging galaxies by first training and implementing a convolution neural

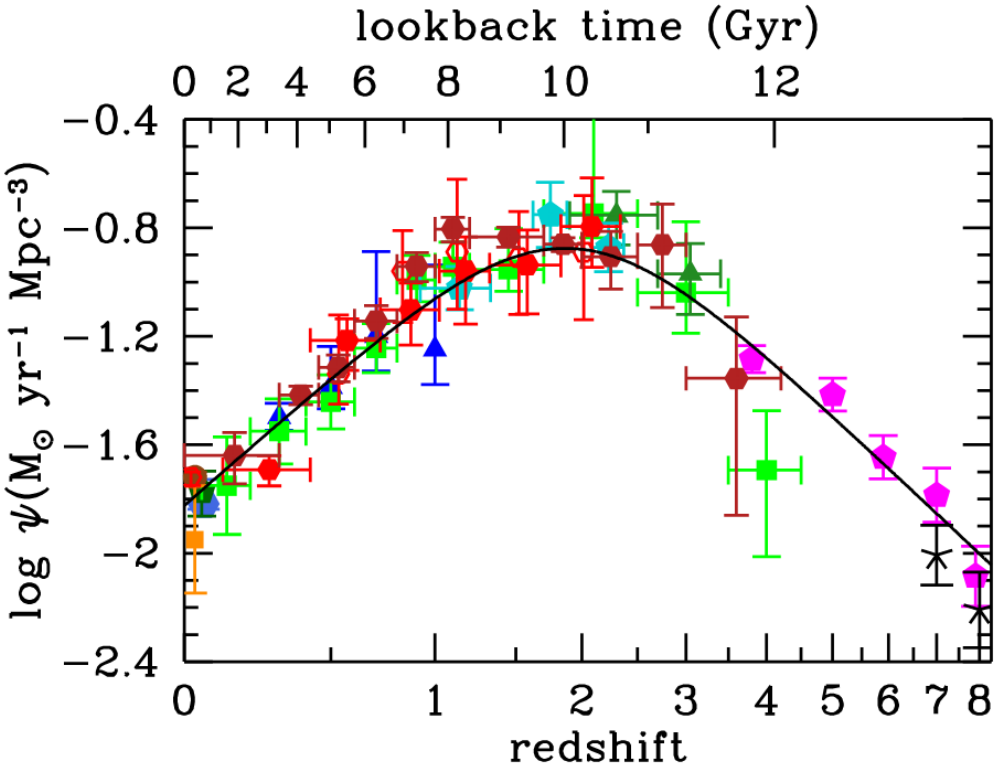

Figure 1.1: Historic star formation rate density (SFRD) as a function of redshift. Taken from Madau and Dickinson (2014). The plot shows that the SFRD is at a peak at $z \sim 2$.

network to identify mergers. The SFR from the merging and non-merging galaxies are then compared after subtracting the main sequence (MS) SFRs. The main sequence of galaxies are the galaxies typical SFR as a function of stellar mass and redshift, as illustrated in Figure 1.2. Pearson et al. (2019) concludes that galaxy mergers have little effect on the average SFR, with a change by a factor of 1.2. They do however find an increase in merger fractions as a function of distance above the galaxy MS. This is used to further conclude that galaxy mergers can induce starbursts.

Starbursts are periods of intense star formation, and have been observed in correlation with mergers. This has resulted in the prevailing theory that most merging galaxies go through a starburst phase (Joseph and Wright (1985) and Schweizer (2005)). However, merger-induced starbursts are more recently found to be the minority of merging systems (Pearson et al. (2019)). Mergers that are more gas rich are able to support higher SFRs and are therefore more likely to host starbursts than gas poor mergers (Lin et al. (2008), Perez et al. (2011) and Naab et al. (2006)). In addition to being a potential cause for increased SFR and starbursts, galaxy mergers contribute to the growth of supermassive black holes (SMBH) at the center of galaxies and active galactic nuclei (AGN) activity. These topics will be explored in the next sections.

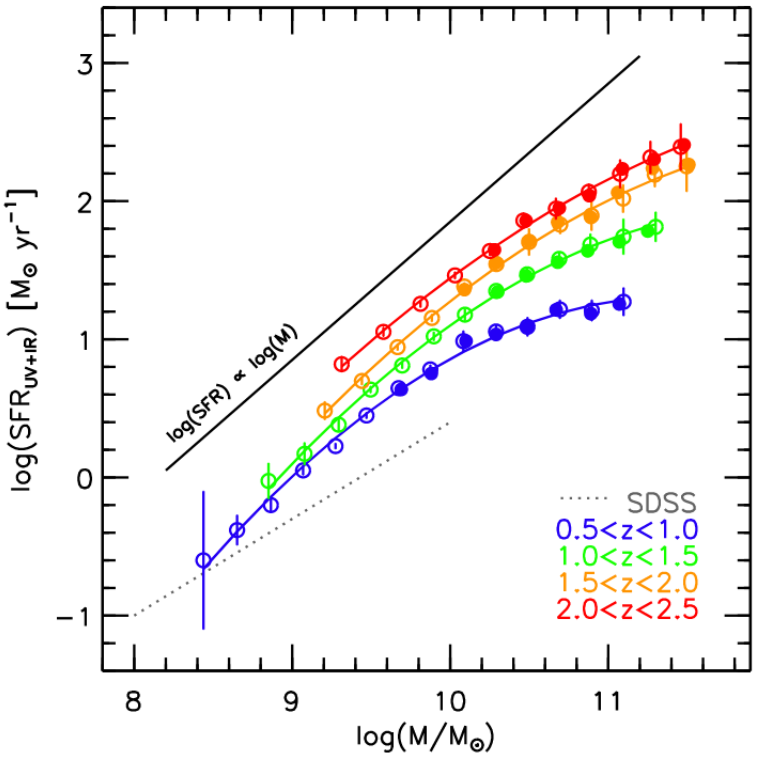

Figure 1.2: The figure shows the main sequence plane for galaxies, showing the typical SFR of galaxies as a function of stellar mass and redshift. Taken from Whitaker et al. (2014).

1.1.2 Galactic outflows as a manifestation of AGN and star formation feedback

The formation of high mass stars ($> 8M_{\odot}$) can impact the evolution of a galaxy through powerful outflows, stellar winds, expansion of HII regions and large amounts of radiation (Murase et al. (2022). AGNs emitting tremendous amounts of energy can redistribute the gas reservoirs in a galaxy and even expel gas out into the IGM.

SMBHs are present at the center of most large galaxies and are the cause of the AGN phenomenon by heating up the accreting gas which then radiates away its heat (Ferrarese and Ford (2005)). The rate of this heat being radiated away is given by Equation 1.1,

$$L = \epsilon_r \dot{M}_{acc} c^2 \simeq 5.7 \times 10^{45} (\epsilon_r / 0.1) (\dot{M}_{acc} / M_{\odot} \mathrm{yr}^{-1}) \mathrm{erg\ s}^{-1} \tag{1.1}$$

where ϵ_r is the radiative efficiency and $\dot{M}_{acc}$ is the rate of mass accretion into the SMBH (Veilleux et al. (2020)) .

AGNs are some of the brightest and yet stable objects in galaxies, with luminosities that can range from 10^6 to $10^{13} L_{\odot}$ (Fabian (1999)) powered by SMBHs with masses in the range $10^4 - 10^{10} M_{\odot}$ (Beckmann and Shrader (2012a)). The unification scheme of AGNs introduced by Urry and Padovani (1995) is illustrated in Figure 1.3. The schematic illustrates that line of sight (LOS) and the radio loudness are the two main parameters in deciding what type of AGN we observe. The orientation of the LOS determines the detectability of the central engine and the broad region of the optical domain, while the degree of radio loudness indicates if a significant jet is produced by the AGN (Beckmann and Shrader (2012a)). The gas accreting into the SMBH forms a hot, thick and optically thin disk around the SMBH. The schematic also illustrates that there is a torus made of dust surrounding the accretion disc. The dusty torus' ability to absorb radiation can cause the AGN to be completely obscured from an observer with certain LOSs (Netzer (2015)). There are two types of AGN feedback, radio mode and quasar mode. The quasar mode of AGN feedback, which is considered radiatively efficient, is the result of short periods of gas accretion which can cause large amounts of energy being injected into the surrounding gas, thereby generating powerful outflows. The radio-mode which is radiatively inefficient, is characterized by slow gas accretion into the SMBH causing radio jets that inject energy into the interstallar medium (ISM).

Feedback is a critical part of the evolution of galaxies, and gas outflows are one of the most clear manifestations of feedback. Models trying to describe the evolution we observe in galaxies invoke feedback from AGNs and starbursts to explain the properties we observe in galaxies (Cazzoli (2017)). Models without a strong AGN feedback contribution estimate much higher SFRs and higher galaxy masses than observed (Hopkins et al. (2006)). This suppression of star formation from AGN feedback is thought to play a role in the lack of overmassive galaxies in the local population of massive galaxies. Stars are formed from molecular gas and therefore outflows in this phase can directly affect star formation. The molecular gas phase is also of interest because it has been found to dominate the outflow mass (Fluetsch et al. (2019) and references therein).

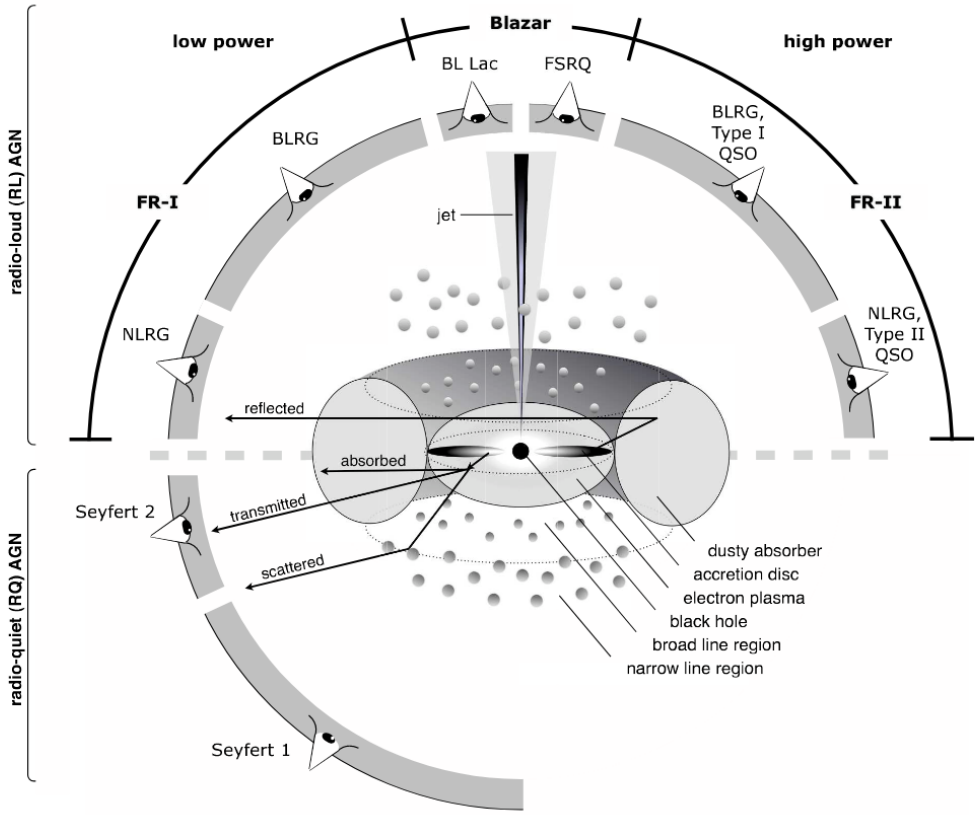

Figure 1.3: A schematic representation of the understanding of Beckmann and Shrader (2012b) for the AGN phenomenon in the unified scheme. The type of object observed depends on viewing angle, whether or not the AGN produces significant jet emission, and how powerful the central engine is. Taken from Beckmann and Shrader (2012a).

D_L (Mpc)	SFR ($M_\odot \mathrm{yr}^{-1}$)	$\log(L_{AGN})$ (erg s^{-1})	$\log(M_*)$ ($M_\odot$)	α_{bol}	$\log(M(H_2))$ ($M_\odot$)
605	330	≤ 42.93	11.10	≤ 0.0007	9.95

Table 1.1: Literature data on IRAS 20100 -4156. D_L: luminosity distance, SFR: star formation rate, L_{AGN}: AGN luminosity, M_*: stellar mass, α_{bol}: fraction of bolometric luminosity from AGN ($\alpha_{bol} = L_{AGN}/L_{bol}$), $\log(M(H_2)$: molecular gas mass. Reference: Fluetsch et al. (2019) and references therein.

1.2 IRAS 20100 -4156

This section presents some background on the source studied in this thesis. The galaxy IRAS 20100 -4156 is a local ultra luminous infrared galaxy (ULIRG) at redshift, $z = 0.129583$ and SFR = 330 (Fluetsch et al. (2019)), and is a product of a merger. It has been classified as an interacting system with two disks by Duc et al. (1997), which is illustrated by Figure 1.4. The galaxy has been classified as an optical type HII galaxy according to Fluetsch et al. (2019) and Veilleux et al. (2009) & 2013, and as a low-ionization nuclear emission-line region (LI(N)ER) by (Perna et al. (2021). HII galaxies are characterised by low metallicities and high concentration of ionised and neutral Hydrogen. HII galaxies are often very luminous starburst galaxies. LI(N)ER galaxies relative to the HII galaxies, have higher metallicities, i.e. higher concentrations of non-Hydrogen atomic species like Oxygen, Nitrogen and Sulphur.

The Baldwin, Philips & Terlevich (BPT) diagram used by Perna et al. (2021) to classify the galaxy can be seen in Figure 1.5. The method uses the relation between spectral line ratios to classify galaxies bases on what the dominant source of ioninizing radiation is. The diagram shows that the northern and southern nuclei are classified as HII and LI(N)ER respectively, indicating that the northern nucleus is more rich in Hydrogen and the southern have a higher metallicity. Table 1.1 reports some basic properties of the source, e.g. AGN luminosity, SFR and stellar mass.

IRAS 20100 -4156 has been studied by several works, most recently by Gowardhan et al. (2018), Fluetsch et al. (2019), Fluetsch et al. (2021) and Perna et al. (2021). The three former articles studied the extent, velocity and mass rates of the galactic outflows hosted by this source, probing the molecular, neutral and ionized phases. A summary of their results can be found in Table 1.2. From the results listed we can see that the molecular gas phase seems to be smaller in extent than both the ionized and neutral gas phases. The molecular gas phase being the only with two sets of results reported, vary significantly, especially in the outflow velocity and the outflow mass rate. The co-variation of these are natural as the outflow mass rate is linearly dependant on the outflow velocity ($\dot{M}_{outf} \propto v_{outf}$). Both articles uses the same ALMA observation considered in this thesis, as well as the CO(1-0) line to trace the molecular gas phase.

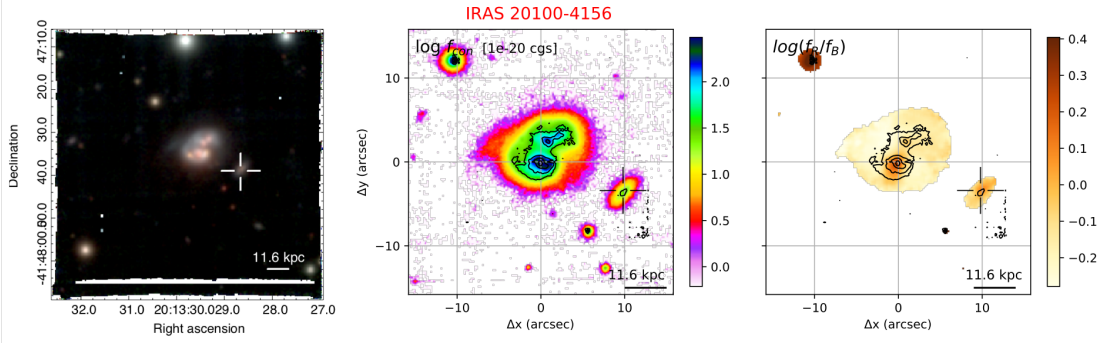

Figure 1.4: Illustrative images of IRAS 20100-4156 taken from Perna et al. (2021). The left panel is a color-composite optical image showing [OIII](green, from the wavelength range 4985-5022 Å rest-frame), Hα (red, 6554-6579 Å), and continuum (blue, 4450-4600 Å). The middle panel displays a continuum image from MUSE (red, 7500-7700 Å) with contours from HST/F160W. The right panel is a stellar continuum colour map obtained from MUSE by dividing the red continuum image (central panel) by a blue image obtained by collapsing the stellar emission in the range 4450-4600 Å. This image also plotted together with the HST/F160W contours. IRAS 20100-4156 companion is displayed with a cross in all panels. The images show that the galaxy has two nuclei.

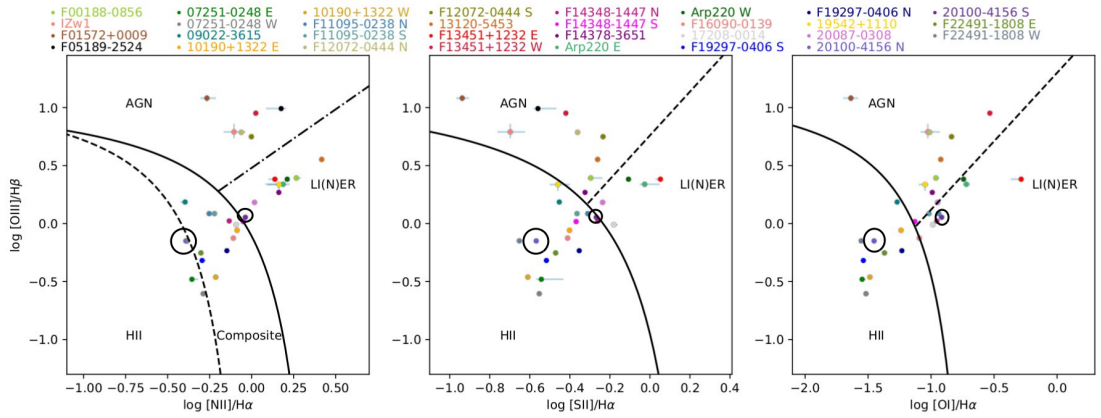

Figure 1.5: BPT diagram from Perna et al. (2021). The galaxy is divided in to a southern and a northern region and classified separately. Perna et al. (2021) studies a sample of galaxies, but the two IRAS 20100-4156 regions are circled. For all three panels the left circle represents the northern region, while the right region is represented by the right circle in all three panels. The northern region is classified as a HII starburst galaxy in all panels, while the southern region is classified as LI(N)ER, HII, LI(N)ER (left to right).

Phase	R_{outf}	v_{outf}	$log(M_{outf})$	$\dot{M}_{outf}$	ref.
	(kpc)	(km s^{-1})	$M_\odot$	($M_\odot$yr^{-1})	
(1)	(2)	(3)	(4)	(5)	(6)
Molecular	0.663	456	9.31	1457	α
Ionised	3.2	900	9.06	130	β
Neutral	1.6	123		61.1	β
Molecular	1.0 ± 0.2	929		672	γ

Table 1.2: Literature data on outflow: (1) outflow phase, (2) outflow radius, (3) outflow velocity, (4) outflow mass, (5) outflow mass rate, (6) references. α: Fluetsch et al. (2019), β: Fluetsch et al. (2021), γ: Gowardhan et al. (2018).

1.3 This work

The focus of this thesis will be to use spectral lines in optical and millimeter observations to study the kinematics and extent of the multi-phase outflowing gas in IRAS 20100 -4156. I will do this by dividing up the region around the central AGN and study the nature of the outflows in both the molecular and ionized gas phase as a function of distance to the galactic centre.

In chapter 2 I will go through the observations used and the methods of cleaning and continuum subtracting the data. Furthermore, I will describe the specifics of dividing the central area around the galactic centre into regions. The results from the subsequent process of fitting multiple Gaussian components to the spectral lines contained in the spectra extracted from these regions will be covered in chapter 3. This section also covers the analysis of the kinematics and estimation of the molecular outflow rate. Discussion of results is presented and in chapter 4 and conclusions are subsequently presented in chapter 5.

Chapter 2

Observations and methodology

This work adopts ΛCDM cosmology with parameters $H_0 = 70\text{km s}^{-1}\text{ Mpc}^{-1}$, $\Omega_M = 0.27$ and $\Omega_\Lambda = 0.73$. Archival data from two observatories were analysed. Millimeter interferometric data from the Atacama Large Millimeter Array (ALMA) containing the CO(1-0) spectral line, and optical spectroscopic data from the Multi-unit spectroscopic explorer (MUSE) instrument of the Very Large Telescope (VLT), where the [OIII]5007 line will be used in this work.

2.1 ALMA observations

The ALMA observations are archival data containing the CO(1-0) emission line with rest frame frequency, $\nu = 115.27120180\text{GHz}$ in band 3. The observations were performed in 2014 with the principal investigator being Henrik Spoon. Previous analyses of these data has been reported by Fluetsch et al. (2019) and Gowardhan et al. (2018). Technical information (e.g. project code, frequency coverage, field of view (FoV), angular resolution) can be found in Table 2.1. The data set consists of five subsets. Information on the five subsets can be found in Table 2.2.

The RMS-values listed in this table represent the noise fluctuations in flux density over the spectral dimension. They where estimated from spectra extracted from beam sized apertures centered on the peak pixel in each sub set. The RMS was computed by finding the standard deviation of the flux density of the non-signal (i.e. line-free) spectral bins. The non-signal spectral range chosen are velocities $v < -1000\text{km/s}$ and $v > 1000\text{km/s}$ with respect to the CO(1-0) spectral line.

Project code	Freq. range (GHz)	FoV (arcsec)	Ang. res. (arcsec)	Band	PI
2013.1.00659.S	101.1-103.0	57.6	0.994	3	Spoon

Table 2.1: Table containing basic information about the ALMA observations considered.

Data set	Obs. date	Obs. time (min.)	No. antennas	RMS (mJy)	Median beam (arcsec)
X84187d_X1b0b	14-Jun-2014	75.5	35	0.22974	1.40×1.08
X83b318_Xcda	09-Jun-2014	41.8	33	0.37202	1.32×1.02
X83f101_X1a0d	12-Jun-2014	75.0	34	0.24910	1.47×1.02
X83f101_X164a	12-Jun-2014	75.2	34	0.25143	1.24×0.96
X8440e0_X4ed	15-Jun-2014	75.3	34	0.24668	1.17×0.97

Table 2.2: Detailed information about the five data subsets of the observations.

2.1.1 Data processing using CASA

To process the five data subsets and make them science ready I used version 6.2.1.7 of the Common Astronomy Software Applications (CASA), McMullin et al. (2007). CASA contains a suite of tools specific to astronomy, and is the go-to software for handling ALMA data. In the next subsections I will describe how I subtracted the millimeter continuum signal from the data to obtain the line measurement, combine them into one data set and cleaned the single concatenated data set.

Continuum subtraction and concatenation

In this thesis I am interested in the line emission contained in the data and therefore want to subtract the continuum emission. The CASA tools contains a module called `uvcontsub`. The module estimates the continuum emission by fitting polynomials to the spectral windows not containing line emission. The model represent the emission for all spectral channels, including the channels containing line emission. For the interval assumed to be free of line emission I chose $[101.159, 101.6]$GHz and $[102.5, 102.937]$GHz. I chose the order of the polynomials to be of the first order.

Once having continuum-subtracted all five data subsets, combined them into one measurement set (MS) before proceeding with the cleaning process. I used the CASA tool `concat` to do this. The product is a single continuum-subtracted measurement set ready to be cleaned.

Cleaning and primary beam correction

The ALMA observations are interferometric observations performed with an array of antennas. Calibrated visibilities was acquired from the ALMA data archive. To convert these data into a science-ready clean image I use the `tclean` tool in the CASA suite. The visibilities are Fourier transformed into an image contaminated by a "dirty beam", making a dirty image. The dirty beam is then deconvolved from the dirty image through an iterative cleaning process, Hogbom (2003). In the task `tclean` I set the parameter `specmode = 'cube'` to create a cube containing two spatial dimensions and one spectral dimension. I chose the pixel size to be 0.1 arcsec and the spectral channel size to be five times the native spectral resolution, resulting in a spectral resolution of 7.2 km/s. Briggs weighting was applied and I chose a robust parameter equal to 0.5. Having deconvolved and cleaned the visibilities therebye creating a measurement set, I used the CASA tool `impbcor` to correct the image for the primary beam pattern. Information on the combined and cleaned data set can be found in Table 2.3.

Data set	Obs. date	Antennas	RMS (mJy)	Median beam (arcsec)	Channel width (km/s)
Combined	9-15. Jun-2014	37	0.11104	1.27×1.05	7.2

Table 2.3: Information on the cleaned measurement set after concatenation of five continuum subtracted visibility subsets and subsequent cleaning.

2.1.2 Grid implementation and extraction of spectra

The first step of my analysis consists in the definition of a spatial "grid" spanning the spatial extent of the CO(1-0) source. The same grid will be applied also to the MUSE data, to enable a spatial comparison between the two tracers. Figure 2.1 shows a map of the total CO(1-0) emission from the galaxy, averaged between -1000 and 1000km/s. Superimposed on the map, I report the grid with box regions indexed left-to-right, bottom-up. The molecular phase center, determined to be in the position of the peak pixel, and used as the galactic centre throughout this thesis, is indicated with a cross. Beam-sized boxes are chosen for the high signal-to-noise areas while slightly larger boxes covering the full extent of the possible outflow are applied for the areas with lower signal-to-noise ratio. The central coordinates and sizes of the boxes can be found in table Table 2.4.

2.2 MUSE observations

The data from the MUSE observations are science-ready archival data from the ESO Phase 3 data archive. The data set has a spectral resolution of 1.25 Å, corresponding to a bin width of 80 km/s. The observatory's seeing is reported to be 0.99 arcsec at the start of the observation and 1.02 arcsec at the end. This resolution of $\sim$ 1arcsec correspond to $\sim$ 2.3kpc with the assumed ΛCDM cosmological parameters. Additional technical parameters of the MUSE data (e.g. spectral range, FoV, instrumental resolution) are listed in Table 2.5. The next subsections will cover the box-grid implementation, continuum subtraction and also an astronomy correction performed on the MUSE cube.

2.2.1 Astrometry correction

By comparing the ALMA and MUSE maps I soon realised that the astrometry of the MUSE data needed correction. Astrometric correction was performed by collaborators of this project using the software Starlink-Gaia (Draper et al. (2014)). We used the Gaia catalogue and selected four stars (with well defined and known positions) included in the MUSE FoV of the data to tweak the astrometry across the entire field. We verified that the position of the source (IRAS 2100 -4156) in the resulting corrected image, matched the position in the ALMA data cube.

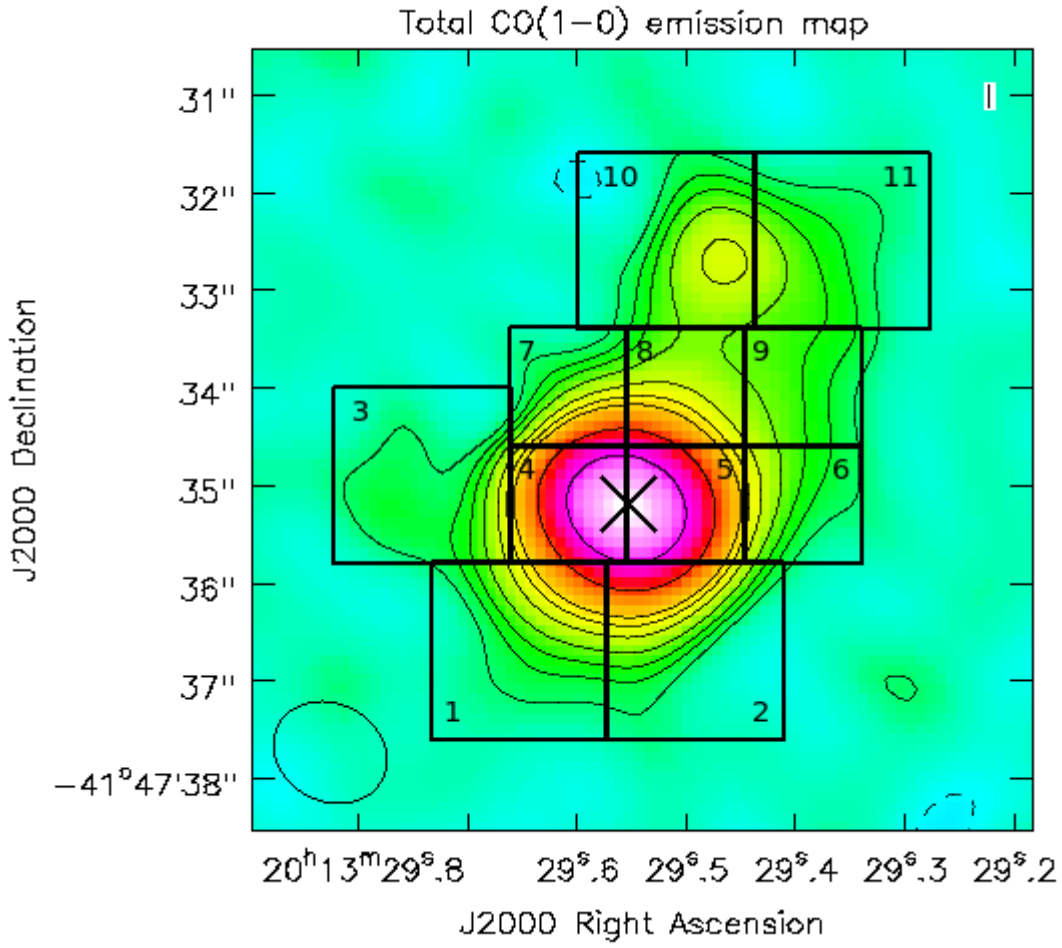

Figure 2.1: Box-grid superimposed on a total emission map of the CO(1-0) line collapsed in the velocity interval [-1000, 1000] km/s. Contours are placed at [-3, 3, 5, 7, 10, 15, 20, 25, 50, 100]σ. Phase center for the molecular gas phase is marked with a cross.

Box no.	(x, y)-coordinates (J2000)	Box size (arcsec)
box 1	(20:13:29.652, - 41.47.36.680)	(1.8 x 1.8)
box 2	(20:13:29.491, - 41.47.36.680)	(1.8 x 1.8)
box 3	(20:13:29.741, - 41.47.34.880)	(1.8 x 1.8)
box 4	(20:13:29.607, - 41.47.35.180)	(1.2 x 1.2)
box 5	(20:13:29.500, - 41.47.35.180)	(1.2 x 1.2)
box 6	(20:13:29.393, - 41.47.35.180)	(1.2 x 1.2)
box 7	(20:13:29.607, - 41.47.33.980)	(1.2 x 1.2)
box 8	(20:13:29.500, - 41.47.33.980)	(1.2 x 1.2)
box 9	(20:13:29.393, - 41.47.33.980)	(1.2 x 1.2)
box 10	(20:13:29.518, - 41.47.32.480)	(1.8 x 1.8)
box 11	(20:13:29.357, - 41.47.32.480)	(1.8 x 1.8)

Table 2.4: Central coordinates and box-sizes of the grid applied on the ALMA data cube. The boxes are numbered from bottom to top, left to right.

Project code	Spec. range (nm)	FoV (arcmin)	Instrumental ang. res. (arcsec)	PI
0103.B-0391	470-935.1	1.56	0.831	S. ARRIBAS

Table 2.5: General info on the MUSE archival data.

2.2.2 Grid implementation and extraction of spectra

Because the goal is to compare results of analysis on the spectra extracted from the boxes in the ALMA and MUSE data, I want to apply the same grid to the MUSE cube. The two data sets do not have the same pixel size, which makes it difficult to implement the exact same grid on them. However, because CASA allows using coordinates when placing the boxes, I used the coordinates listed in Table 2.4 to create the box-grid in CASA `viewer`. The difference in pixel size caused the viewer tool to shift some of the values slightly, resulting in the coordinates listed in Table 2.6. The grid, applied to the MUSE data set, is shown in Figure 2.2. The figure shows a total emission map in the spectral region of the [OIII]5007 emission line, containing both line and continuum emission.

The position of the peak pixel in the total CO(1-0) map presented earlier indicates the molecular phase centre, and will in this thesis be used as the galactic centre. The position is indicated with a black cross in both the CO(1-0) and [OIII] map. On comparing the position of the grid relative to the centre position, to the grid applied on the CO(1-0) map in Figure 2.1, it is clear that the grid and/or the centre position are slightly off with respect to each other. The distance from each box to the galactic centre is of interest as I will later present parameters determined for each box as a function of this distance. To study the discrepancy more closely, I computed the distance from the center position of each box to the molecular phase centre, for both grids separately. I then estimated the RMS (i.e. square root of variance) of the difference in distance to the centre between the the boxes in the two grids to be < 0.38kpc.

The MUSE spectra were also extracted using the CASA `viewer`. This tool collapses the spatial dimensions of the cube in each cube by taking the mean. Because I am interested in the line emission I want to subtract the continuum emission, which in the optical wavelength range probed by MUSE traces the stellar component of the galaxy. In the next subsection I will explain how I performed the continuum subtraction on the MUSE spectra.

2.2.3 Continuum subtraction

In this section I will explain the methods by which I subtracted the stellar continuum from the MUSE spectra extracted from the box-grid as described in Sec. 2.2.2. To model and fit the continuum I used the penalized pixel-fitting method (pPXF) based on the method described in Cappellari and Emsellem (2004) which were later improved in Cappellari (2017). The pPXF software fits stellar and gas templates to the observed spectrum. Based on these fits, the software is able to model the stellar continuum which I then subtract from the observed spectrum. An illustration of the results from the fitting process are shown in Figure 2.3 where the continuum is modeled and fitted to the spectrum in box region 1, which is located to the south west of the dominant nucleus. The spectral lines detected and included in the gas templates in the pPXF fitting process are illustrated in this figure. Table 2.7 lists the spectral lines with their respective rest frame wavelengths.

Box no.	(x, y)-coordinates (J2000)	Box size (arcsec)
box 1	(20:13:29.652, - 41.47.36.677)	(1.8 x 1.8)
box 2	(20:13:29.491, - 41.47.36.677)	(1.8 x 1.8)
box 3	(20:13:29.741, - 41.47.34.877)	(1.8 x 1.8)
box 4	(20:13:29.607, - 41.47.35.177)	(1.2 x 1.2)
box 5	(20:13:29.500, - 41.47.35.177)	(1.2 x 1.2)
box 6	(20:13:29.393, - 41.47.35.177)	(1.2 x 1.2)
box 7	(20:13:29.607, - 41.47.33.977)	(1.2 x 1.2)
box 8	(20:13:29.500, - 41.47.33.977)	(1.2 x 1.2)
box 9	(20:13:29.393, - 41.47.33.977)	(1.2 x 1.2)
box 10	(20:13:29.518, - 41.47.32.477)	(1.8 x 1.8)
box 11	(20:13:29.357, - 41.47.32.477)	(1.8 x 1.8)

Table 2.6: Central coordinates and box-sizes of the grid applied on the MUSE data cube. The boxes are numbered from bottom to top, left to right.

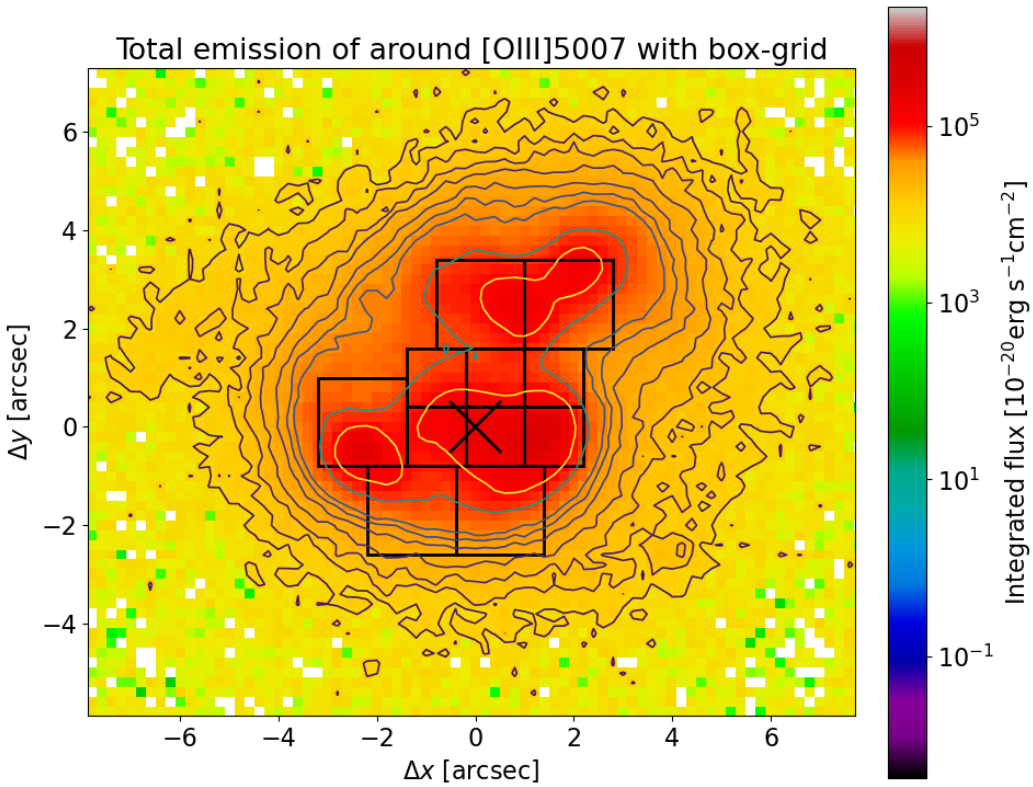

Figure 2.2: Box-grid superimposed on total emission map in the spectral region of the [OIII]5007 emission line ($\lambda \in [5650, 5665]$Å), containing both line and continuum emission. Contours at levels [-3, 3, 5, 7, 10, 15, 20, 25, 50, 100]σ. The coordinates are relative to the molecular phase center estimated as the peak pixel in the total emission map of the CO(1-0) line indicated by a black cross.

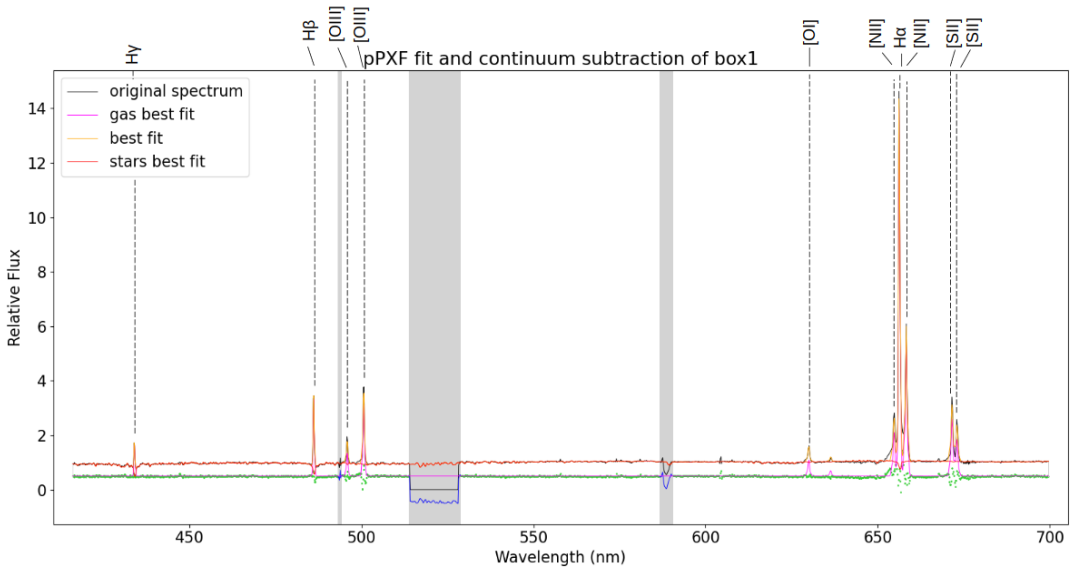

Figure 2.3: pPXF fit and modeling of the spectrum extracted from box 1 which is located south west of the dominant nucleus. The black line (mostly hidden by the fit) is the relative flux of the observed spectrum. The red line is the pPXF fit for the stellar component, while the orange line is a fit to the gas emission lines. The green symbols at the bottom are the fit residuals, while the blue lines is the gas-only best-fitting spectrum. The spectral lines detected in the pPXF fit are marked and named above the plot. The shaded areas are excluded from the fitting process. The masked area $\lambda \in [5500, 6000]$Å contains a spectral line not accounted for in the fitting process (i.e. the NaID absorption doublet), and was therefore masked.

Emission line	Wavelength (Å)
Hα	6562.80
Hβ	4861.33
Hγ	4340.47
[SII]6716	6716.47
[SII]6731	6730.85
[OIII]5007d	5006.84
[OI]6300d	6300.30
[NII]6583d	6583.41

Table 2.7: Emission lines detected in the pPXF fit with corresponding rest frame wavelengths.

I will now explain the technical aspect of how I used the pPXF software to subtract the continuum from each of the box-spectra. In the following description I refer to the analysis performed on the spectrum extracted from box region 1 for illustrative purposes, but the same steps are applied to all regions of the grid. First I corrected the wavelength scale for redshift using the relation shown in Equation 2.1, which relates the obseved wavelength to the wavelength of the emitted light as a function of redshift.

$$\lambda_{emit} = \frac{\lambda_{obs}}{(1+z)} \tag{2.1}$$

The next step is to determine the spectral range to be considered for the fitting process. The spectral upper bounds was set conservatively to 7000Å because the pPXF fitting failed in the spectral window $[7200, 7500]$Å as is shown in Figure 2.4. The same figure also shows that the MUSE archival data contain a non-signal interval in the range $\lambda \in [5139, 5287]$Å. This spectral window was therefore masked and excluded from the fitting process. Some of the boxes contain spectral lines not detected by the pPXF model and fitting process in the spectral windows $[4934, 4943]$ & $[5867, 5905]$Å, hence these were masked. The RMS for each box-spectrum was estimated using the spectral intervals $[4400, 4800]$ & $[5290, 5870]$Å. These intervals are chosen because they are in the vicinity of the [OIII] line I am interested in studying. I first determined the RMS in each of the two spectral windows by finding the standard deviation of the flux density. The RMS for the full spectrum for the box was then estimated to be the mean of the RMS in the two spectral windows.

An illustrative continuum subtracted spectrum, zoomed in on the [OIII]5007 emis-

sion lines is shown in Figure 2.5. In the next Chapter I will describe the following steps, that consist in the identification and study of the outflowing components in both the ALMA and MUSE data.

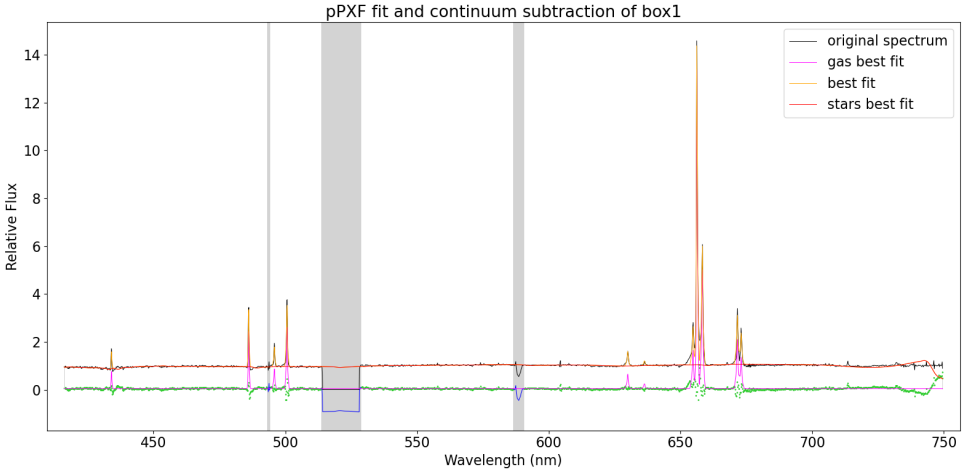

Figure 2.4: Example output plot from the pPXF fitting process using the observed spectrum from box 1 located to the south west of the galactic centre. This plot illustrates that the fit fails in the spectral window $\lambda \in [7200, 7500]$Å. The areas shaded in grey are the masked spectral windows not included in the fits. The green data-points are the residuals of the best fit with respect to the observed flux density.

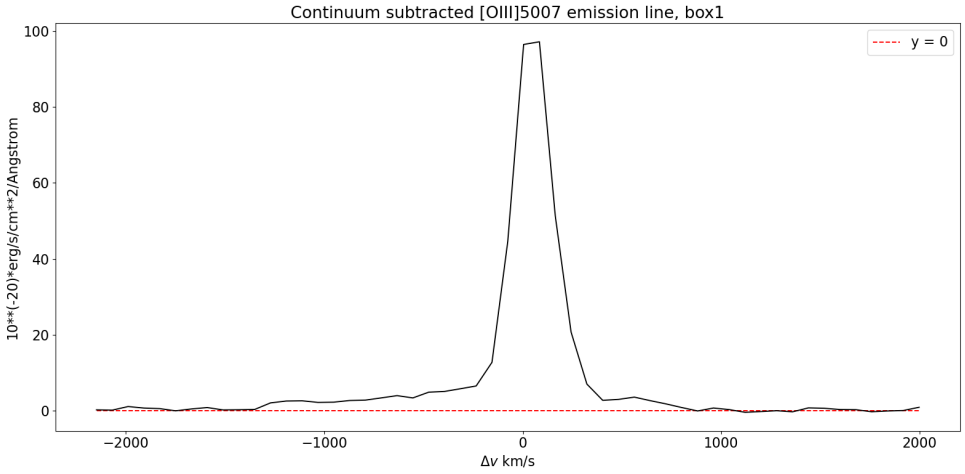

Figure 2.5: Continuum subtracted spectrum from box 1 zoomed in on the [OIII]5007d emission line.

Chapter 3

Results

This chapter covers the process of fitting of multiple Gaussian components to the CO(1-0) and [OIII]5007 emission line spectra, tracing molecular and ionised gas respectively. For each for the two tracers, and for each box, I fitted the emission line profile with multiple Gaussian profiles. The fit components are then used to detect gas outflows subsequently study the gas kinematics in both phases and estimate the outflow mass rates for the molecular gas phase.

3.1 Spectral line fitting

This section covers the spectral analysis performed by fitting multiple Gaussian components to the nebular [OIII]5007d line observed by MUSE, tracing the ionised gas, and CO(1-0) line observed by ALMA, tracing the molecular gas. An integrated spectrum was extracted from each box (i.e. summing the contribution from all pixels contained in each box), resulting in 11 CO(1-0) and 11 [OIII] spectra. All spectra show some anisotropies and deviations from a single-Gaussian profile, thanks to the high S/N of the data and the presence of widespread outflow in this source. This implies that I will need to use multiple components to fit each spectrum. To determine whether the fit requires two of three Gaussian components I initially planned to fit each of the eleven spectra containing the CO(1-0) line with both two and three Gaussian components and compare the results. I would choose the number of components yielding the best fit of the CO(1-0) line for each box region and subsequently fit the eleven spectra containing the [OIII] line extracted from the box regions in the MUSE observations with the same number of components. It turned out however, as I will illustrate, that the number of components resulting in the best fit for the CO(1-0) line failed to detect some clear cases of outflow in the [OIII] line.

In order to evaluate the fitting results and determine what number of components are best for each box, I decided to use a statistical criterion. It is natural to evaluate the χ^2 because it is the parameter that is minimized in order to obtain the fit in the first place. When comparing fits with a different number of parameters however, overfitting is a concern. To overcome the problem of overfitting I chose to evaluate the Bayesian

information criterion (BIC) in addition to the a reduced χ^2. The BIC parameter is described as,

$$BIC = \chi^2 + k\ln(n) \tag{3.1}$$

where k is the number of parameters and n is the number of data points. The BIC parameter penalizes adding parameters to a model and thereby reduces the risk of overfitting. The reduced χ^2 is described as,

$$\chi^2_{red} = \frac{\chi^2}{df} = \frac{1}{df}\sum_i^n \frac{(O_i - C_i)^2}{\sigma^2} \tag{3.2}$$

where df is the number of degrees of freedom, $df = n - n_{par}$, where n_{par} is the total number of parameters in the model applied. O is the observed value, C is the model value and σ is the RMS. The RMS is computed for each box-spectrum similarly to how I computed the RMS at the beginning of this chapter. The RMS computed for each box region is assumed to be the same value for all spectral bins.

The BIC, reduced χ^2 and re-bin factor for each of the CO(1-0) fits are listed in Table 3.1. The ease the reading if this thesis, the plots showing the comparison between the 2- and 3-component fitting for each of the CO(1-0) spectra are reported in the Appendix of this thesis. The BIC suggests that it is best to fit two components to the CO(1-0) spectral extracted from boxes $1, 3, 6, 7, 8, 9, 10, 11$, and three components to boxes $2, 4, 5$. The fitting of both two and three Gaussian components to the CO(1-0) emission line in box region 1 is illustrated in Figure 3.1.

Having determined what number of Gaussian components to fit the CO(1-0) line in the ALMA data, I fitted the [OIII] line contained in the MUSE spectra extracted from their respective box regions, with the same number of components. Using the same number of Gaussian components in fitting the [OIII] line as used in the CO(1-0) fit, resulted in outflow being undetected. Figure 3.2 presents the fit of two Gaussian components to the CO(1-0) and [OIII] lines in the box 2 region. The figure shows that the [OIII] fit has a $\chi^2_{red} = 5.914$ and residuals significantly larger than 1σ in an approximate velocity interval of $[-1500, -200]$km/s. This led me to conclude that I can not blindly fit the [OIII] line with the same number of Gaussian components used in the CO(1-0) fit. I therefore perform a quality of fit comparison similar to the one I did for the CO(1-0) line. Table 3.2 lists the reduced χ^2 and BIC for the fits of both two and three Gaussian components to the [OIII] line for each box region. All the plots illustrating the [OIII] comparison fitting can be found in the Appendix. The BIC criterion and an inspection of the residuals shows that a 3 component-fit is preferred over a 2-component one for all boxes, in the case of the [OIII]5007 emission line. Three Gaussian components will therefore be used in the fitting of the [OIII] line for all box regions. The final fits of both the CO(1-0) and [OIII] line for all box regions are presented in figures 3.3, 3.4 and 3.5.

Box no.	2 comp.	2 comp.	3 comp.	3 comp.	Re-bin factor
	χ^2_{red}	BIC	χ^2_{red}	BIC	
Box 1	1.213	249.611	1.226	264.086	3
Box 2	1.282	262.190	1.205	260.329	3
Box 3	1.017	214.482	1.012	226.098	3
Box 4	2.439	1384.446	1.711	996.407	None
Box 5	3.394	1911.699	1.286	762.849	None
Box 6	1.068	223.673	1.056	233.945	3
Box 7	1.086	226.776	1.096	241.047	3
box 8	1.049	220.111	1.057	234.086	3
Box 9	1.018	214.508	0.981	220.603	3
Box 10	1.166	241.233	1.380	291.367	3
Box 11	1.085	330.005	1.184	370.302	2

Table 3.1: Table listing the reduced χ^2, Bayesian information criterion (BIC) and re-bin factor for the Gaussian fits of two and three components on the CO(1-0) line.

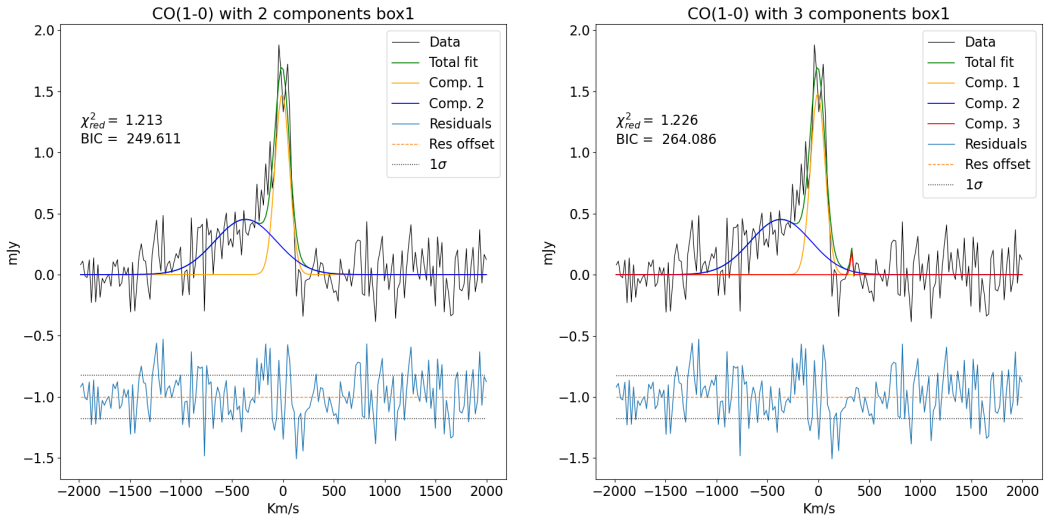

Figure 3.1: Figure illustrating the multi component fit of the CO(1-0) line. Both figures show the observed flux density in black and the total fit in green while the Gaussian components are shown in yellow and blue for two components and red is added as the third component. The residuals, offset around the horizontal orange line are plotted in light blue below the data and models. The 1σ threshold is shown in the black dashed lines.

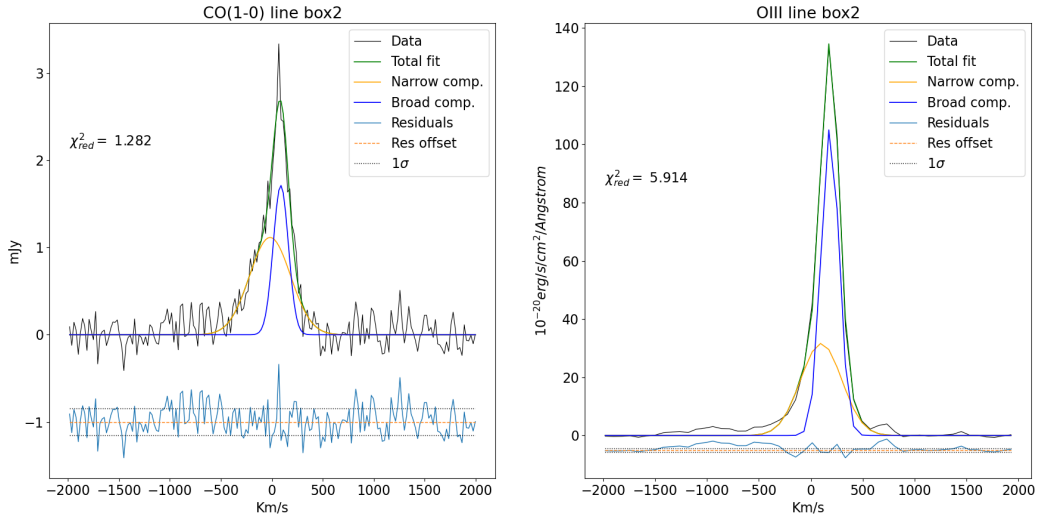

Figure 3.2: Two Gaussian components are fitted to both the CO(1-0) (left panel) and the [OIII] line (right panel). The residuals are offset and plotted below the fit with a 1σ threshold. The fit of the [OIII] line is clearly unsuccessful in capturing parts of the blueshifted outflow component. The $\chi^2_{red} = 5.914$ and the residual plot consistently showing residuals $> \sigma$ for $\Delta v \in [-1500, -200]$km/s

Box no.	2 comp.	2 comp.	3 comp.	3 comp.
	χ^2_{red}	BIC	χ^2_{red}	BIC
Box 1	3.099	159.810	0.912	72.601
Box 2	5.914	283.667	1.718	105.748
Box 3	2.823	147.663	2.395	133.415
Box 4	1.785	102.006	0.654	62.010
Box 5	8.239	385.984	1.300	88.500
Box 6	16.233	737.719	11.850	521.073
Box 7	1.809	103.075	0.818	68.760
box 8	6.639	315.595	2.236	126.885
Box 9	6.280	299.806	4.830	233.253
Box 10	2.314	125.300	1.236	85.870
Box 11	3.619	182.708	2.607	142.089

Table 3.2: Table listing the reduced χ^2 and Bayesian information criterion (BIC) for the fitting of two and three Gaussian components to the [OIII] line for each box-spectrum. The BIC is consequently lower for the fits with three components. The reduced χ^2 is large for boxes 6 and 9.

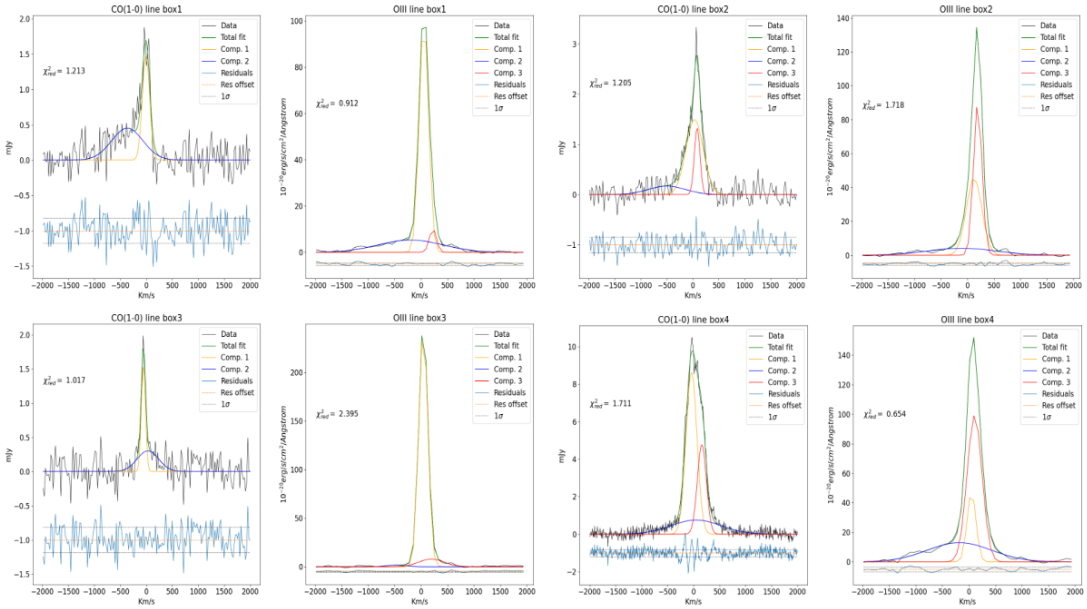

Figure 3.3: Results of the fitting process of the CO(1-0) and [OIII] lines for box regions 1-4. The CO(1-0) line is fitted with two components for box region 1 and 3. Three component are fitted to the CO(1-0) line in box regions 2 and 4, and box regions 1-4 for the [OIII] line.

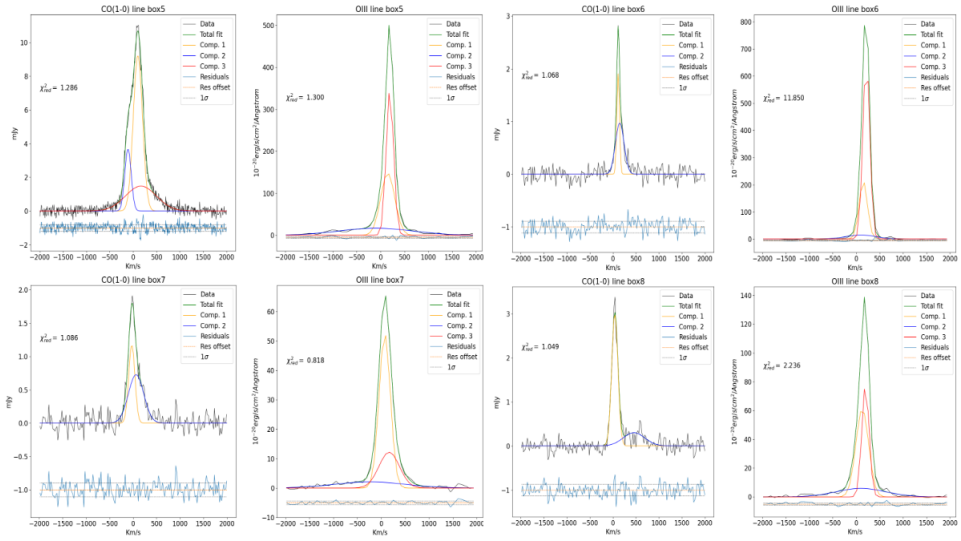

Figure 3.4: Results of the fitting process of the CO(1-0) and [OIII] lines for box regions 5-8. Two Gaussian components are fitted to the CO(1-0) line in box regions 6-8. Three components are fitted to the CO(1-0) line in box region 5 and to the [OIII] line in box regions 5-8.

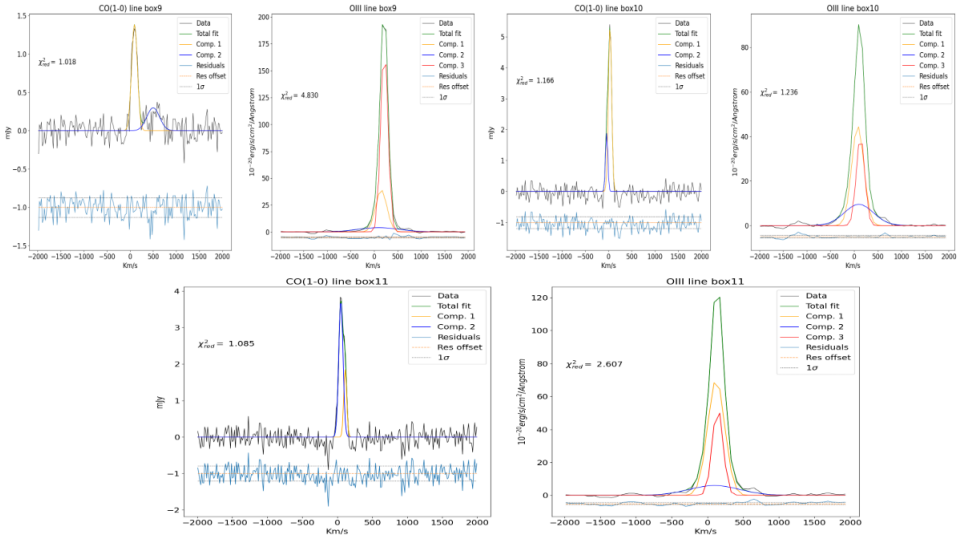

Figure 3.5: Results of the fitting process of the CO(1-0) and [OIII] lines for box regions 9-11. Two and three components are fitted to the CO(1-0) and [OIII] line in box regions 9-11 respectively.

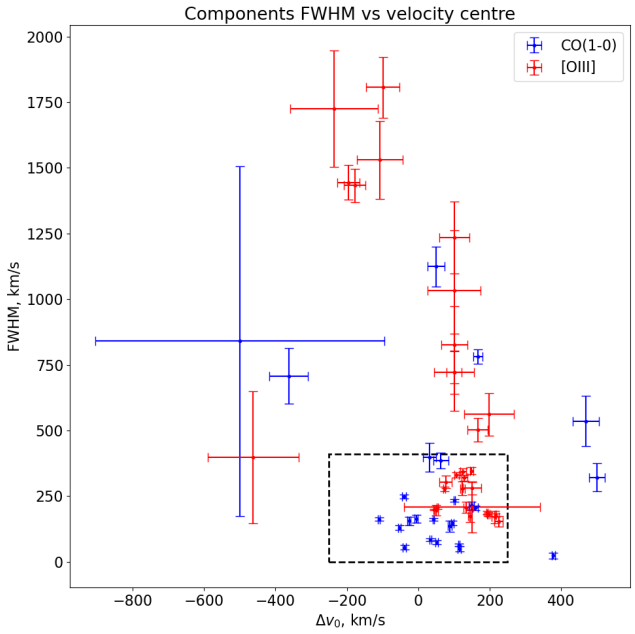

Figure 3.6: The FWHM as a function of central velocity for each Gaussian component. The dashed rectangle encompasses the parameter space region that I identify as tracing non-outlfowing components. The rectangle boundaries are $[-250, 250]$km/s for Δv_0 and $[0, 410]$km/s for the FWHM.

3.2 Outflow analysis

Having fitted the CO(1-0) and [OIII] line spectra extracted from each of the box regions with their respective optimal number of Gaussian components, I will in this section describe the methods used to determine which components show signs of outflow. I will then use this information to study the outflow velocity for both the CO and [OIII]-emitting gas, and to derive estimates of the molecular outflow rates.

To determine if a component represents outflowing gas I implement a method to classify the components similar to what Cicone et al. (2018) applied to the NGC6240 molecular line observations. Figure 3.6 shows the FWHM of each Gaussian component plotted against the corresponding central velocity relative to the spectral line rest frame. There is a clear clustering of components with both low central velocities and small velocity dispersions (FWHMs). Choosing the non-outflow space as $\Delta v_0 \in [-250, 250]$km/s and FWHM $\in [0, 410]$km/s nicely classifies these as non-outflow components and all other components as outflow components. This is consistent with the boundaries chosen by Cicone et al. (2018) on a different (U)LIRG, NGC6240. The observed clustering of the spectral line components and the similarities between the CO(1-0) and [OIII] components is quite striking, and shows that this method can possibly be applied to identify outflows in these kinematically and morphologically complex sources such as (U)LIRGs.

3.2.1 Molecular outflow mass rates

In this section I will describe the method of estimating the molecular outflow mass rates. The mathematical basis for the outflow mass rate is described in Equation 3.3,

$$\dot{M}_{outf} = \frac{M_{outf}}{\tau_{dyn}} = \frac{M_{outf} v_{outf}}{r_{outf}} \tag{3.3}$$

where M_{outf} is the mass of the ouflowing gas phase, and τ_{dyn} is the dynamical time it takes gas outflows with velocity v_0 to reach distance r_0 from the galactic centre, defined as $\tau_{outf} = r_{outf}/v_{outf}$. The outflow velocity is defined as,

$$v_{outf} = \mathrm{FWHM}_{broad}/2 + |v_{broad} - v_{narrow}| \tag{3.4}$$

where v_{broad} and v_{narrow} are the velocity centroids of the broad and narrow components relative to the spectral line rest frame. This definition of the outflow velocity was taken from Fluetsch et al. (2019). In the cases of three components being fitted to a spectral line, the narrow component is assumed to be the component with the largest amplitude. If there is multiple components from the same box region classified as outflowing, their velocity and subsequent outflow contribution is calculated separately and then added together. The molecular gas mass is calculated using Equation 3.5,

$$M_{outf}(H_2) = \alpha_{CO} L'_{CO} \tag{3.5}$$

where α_{CO} is the CO-to-H_2 conversion factor. I will assume a conversion factor of $\alpha_{CO} = 2.0 \pm 0.4 \left[M_\odot \left(\mathrm{K\ km\ s^{-1} pc^2} \right)^{-1} \right]$, which is the mean value estimated using CO(1-0) and [CI](1-0) line data on 16 local (U)LIRGs by Montoya Arroyave et al. in prep. L'_{CO} is the CO(1-0) luminosity measured in K km s^{-1} pc^2. The CO line luminosity is defined in Equation 3.6.

$$L'_{CO} = 3.35 \times 10^7 \frac{D_L^2}{\nu_{obs}^2 (1+z)^3} \int S_{CO} dv \tag{3.6}$$

The luminosity distance is estimated to be $D_L = 609.9$Mpc using the cosmological parameters assumed at the beginning of chapter 2. ν_{obs} is the observed frequency of the CO(1-0) spectral line, estimated to be 102.04603559Ghz. The integral is the velocity-integrated flux of the CO line in Jy km s^{-1} and can be found to be $\int S_{CO} dv = S_{peak} \sigma \sqrt{2\pi}$, where S_{peak} and σ are the amplitude and standard deviation respectively, of the outflow Gaussian component. Equation 3.6 is taken from Solomon and Vanden Bout (2005).

Chapter 4

Discussion

In this section I used the results of the analysis described in chapter 3 to study the properties of the molecular and ionised outflow components in the target. The velocity components will be considered first, before the outflow mass rates are presented.

The velocities of the gas as described by the parameters of the Gaussian components have already been considered to some degree in Figure 3.6. The figure illustrates the relation between the FWHM of the Gaussian components, and the central velocity with respect to the systemic redshift of the galaxy. The purpose of the figure was to classify the components as either outflow, or non-outflow components, but it also gives a general insight into the distribution and scale of the velocity components. In addition to the apparent clustering described in section 3.2, the [OIII] components show higher FWHM values than the CO(1-0) components, as well as a larger number of components classified as outflow.

Building on this consideration of the components parameters illustrating gas velocity, Figure 4.1 presents the central velocities and standard deviations of all components as a function of distance to the galactic centre (i.e. position of peak pixel in total CO(1-0) emission map). The right panel plotting the standard deviations, show two distinct trends. One trend is the narrow lines with a flat relation with respect to the distance. The broad lines show a trend of decreasing with respect to distance, indicating that the outflow velocities decrease with distance. The [OIII] velocities also seem to be larger than the CO(1-0) velocities. The plot of the central velocities estimated for the molecular gas phase show signs of a peak for $r \sim 3 - 5$kpc. These are components corresponding to box regions 1, 2, 8 and 9. By investigating the fitted components presented in chapter 3, I find that the velocities from box regions 1 & 2 (located to the south) are blueshifted, while velocities from box regions 8 & 9 (located to the north/north-east) are redshifted.

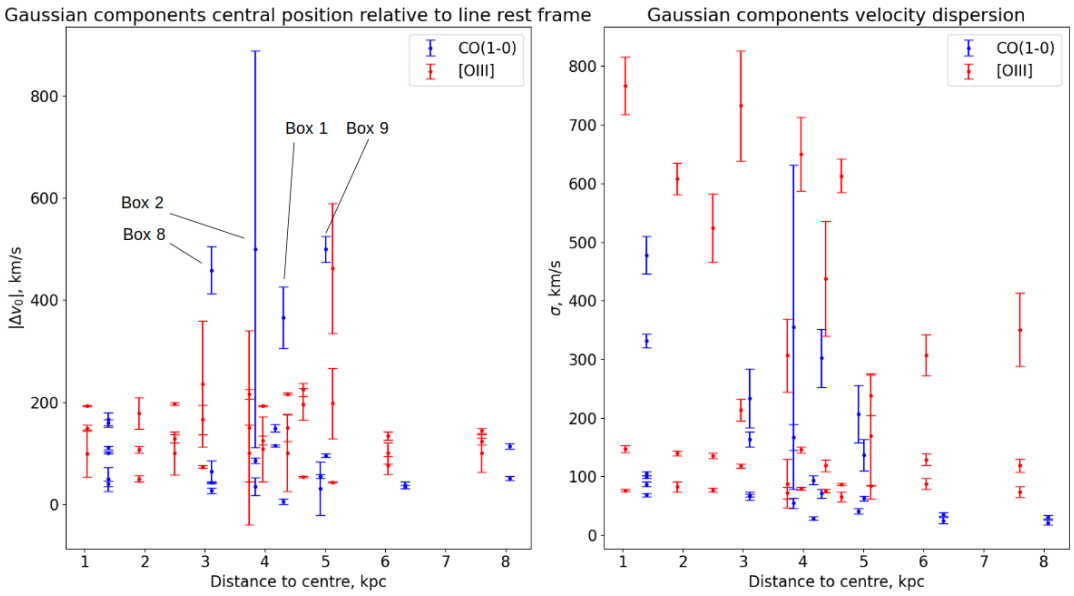

Figure 4.1: Plot illustrating the best it Gaussian kinematics parameters as a function of the distance to the galactic centre. The left panel shows the absolute value of the central position of the Gaussian components with respect to the spectral line rest frame. The right panel shows the velocity dispersion of each Gaussian as a function of the distance to the centre.

Figure 4.2 shows the outflow velocity (defined in Equation 3.4) which combines the information about the relative velocity of a Gaussian (i.e. how fast the gas moves with respect to the galactic dynamic centre) and its velocity dispersion, as a function of distance to the galactic geographical centre. The outflow velocity is computed for all box regions classified as outflow regions. The ionized outflow velocities as traced by the [OIII] line decreases as a function of distance to the galactic centre, and gas outflows are detected as far out as $\sim 7-8$kpc from the centre. The velocity of the molecular outflow traced by the CO(1-0) line does not show signs of dependence of distance to the centre and appear more or less constant as a function of distance. Molecular outflow components are detected out to a distance of $\sim$ 5kpc from the galactic centre. The ionized outflow is found to have significantly higher velocities than the molecular gas in the regions closest to the centre. The average molecular velocity is found to be $v_{OF,avg}(mol) = 650 \pm 60$km/s, while the average ionized outflow velocity is estimated to be $v_{OF,avg}(ion) = 776 \pm 19$km/s. Median velocities are reported to be 651 ± 24 and 710 ± 40km/s for the molecular and ionised phases respectively.

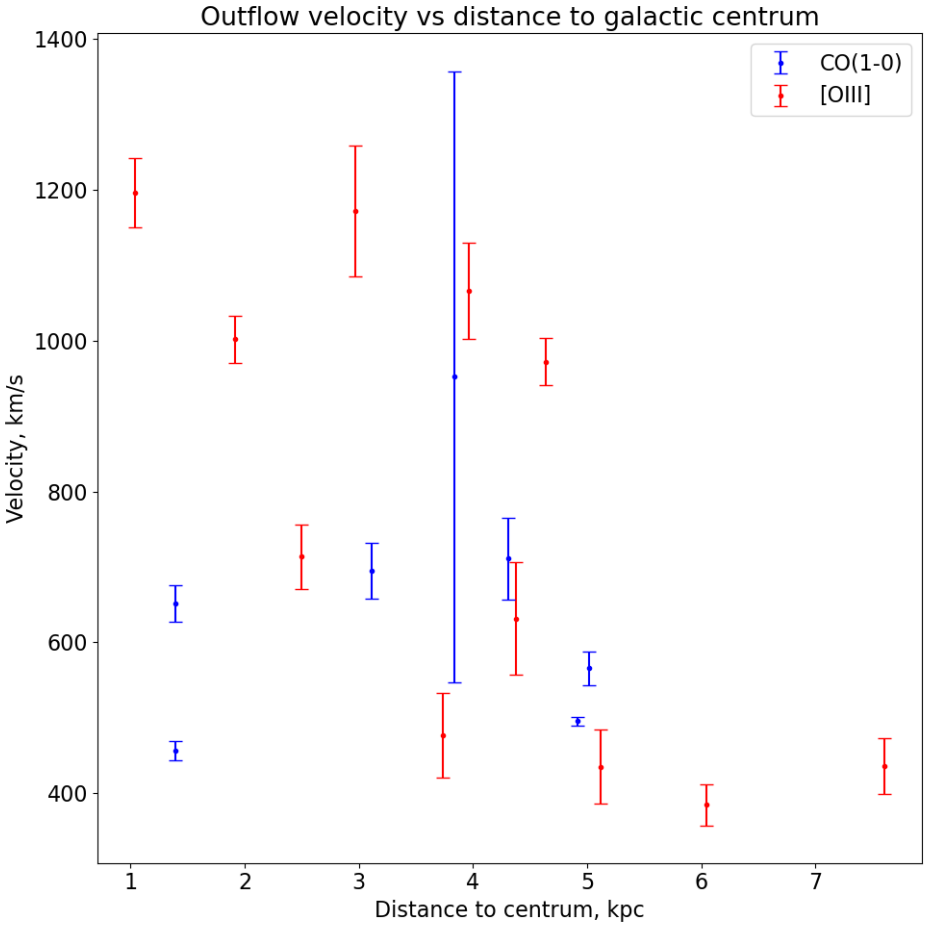

Figure 4.2: The outflow velocity (defined in Equation 3.4) reported as a function of distance to galactic centre.

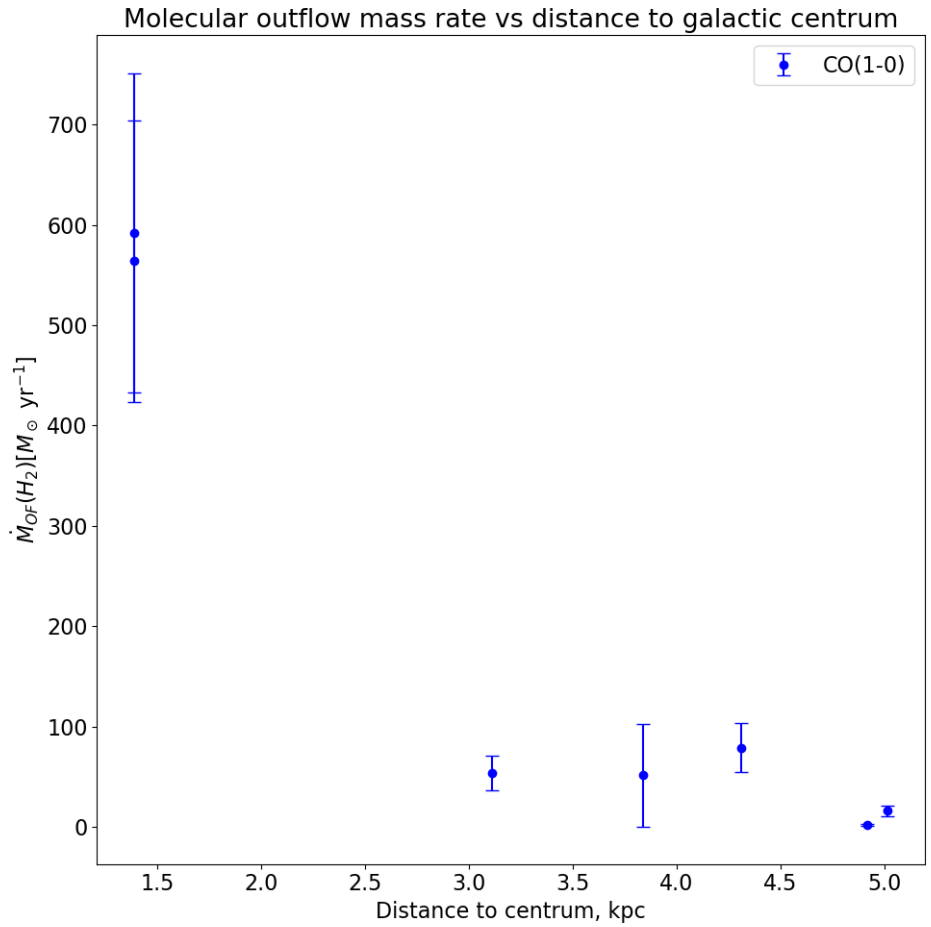

Figure 4.3: Molecular outflow mass rate is plotted as a function of the distance to the molecular phase centre.

Using the assumptions described in subsection 3.2.1, I calculated the molecular outflow rate for each CO(1-0) component considered "outflowing". Figure 4.3 shows the molecular outflow rate as a function of distance to the galactic centre. The two regions nearest the galactic centre, with a distance of $\sim$ 1.5kpc, are found to have the highest rates of molecular outflows. As the distance to the centre increases, the outflow mass rates rapidly decreases to less than $100 M_\odot \mathrm{yr}^{-1}$. This is to be expected as the outflow rate scales as $\dot{M}_{outf} \propto 1/R$, where R = radius (distance to the galactic centre). The combined molecular outflow mass rates from all regions classified as containing outflows is found to be $\dot{M}_{outf}(H_2) = 1360 \pm 340 M_\odot \mathrm{yr}^{-1}$. The total mass of the molecular gas phase classified as outflowing is estimated to be $log(M_{outf}(mol)) = 9.60 \pm 8.99 M_\odot$.

Chapter 5

Conclusions

The galaxy IRAS 20100 -4156 is a local ULIRG undergoing a major merger, and it is characterised by a high SFR and high outflow velocities as reported in previous work. In this MAster thesis, I presented a spatially resolved analysis of the multi-phase outflow characteristics of this source was studied as traced by the CO(1-0) (molecular) and [OIII]5007 (ionised) emission lines.

One of my results is the finding of a persistent presence of CO and [OIII] components with $\sigma \sim 100$km/s at all distances (right panel of Figure 4.1). There appears to be indeed a bimodality, in both the CO and [OIII] gas tracers, where components are mostly either narrow and at low velocity, or broad and high velocity (see e.g. also Figure 3.6). By examining only the velocity of the Gaussian components (see left panel of Figure 4.1), there are no clear signs of such bimodality, but there is a slight peak in central velocities at $r \sim 4$kpc. This peak in central velocity is much more prominent in the molecular gas phase, which may indicate that the molecular gas contain directional outflow as opposed to outflow with uniformly distributed velocities. This directional molecular outflow is located in box regions 1 & 2 (blueshifted) to the south, and 8 & 9 (redshifted) to the north/north-east. This clear opposite directionality of outflow with respect to the galactic centre hosting the AGN, may indicate the presence of relativistic jets.

The outflow velocity (defined in Equation 3.4, including a contribution from both the central velocity and the velocity dispersion of a Gaussian components) is shown in Figure 4.2 as a function of distance from the center of the galaxy. This plot gives insight into the movement of both the molecular and ionised gas phase at different distances to the centre. The two gas phases show clear signs of different kinematics. The molecular gas phase appears to have fairly constant velocities ($v \sim 600$km/s) at all distances. The ionised gas phase shows high velocities near the centre, and rapidly decreasing velocities for $r > 5$kpc. The ionized outflows are also characterized by much higher velocities close to the galactic centre ($\sim 1000 - 1200$km/s) than the velocities at distances greater than ~ 5kpc (~ 400km/s). A possible explanation for this difference in kinematics is that the molecular outflows are driven to a much higher degree by stellar feedback, providing contribution continuously as a function of distance. The ionised outflow, characterised

with declining velocity as a function of distance, is more likely to be driven by a central AGN unable to replenish the outflows as they move outward.

The average molecular outflow velocity of 650 ± 60km/s lies well within the range of velocities reported by Fluetsch et al. (2019) and Gowardhan et al. (2018) of 456 and 929 km/s respectively. The ionised outflow velocities reported by Fluetsch et al. (2021) of 900km/s is slightly larger than the average of 776 ± 19km/s reported in chapter 3, but well within largest velocities reported.

The extent of the observed outflow is larger for the ionised relative to the molecular gas phase. This is consistent with the outflow radii reported by previous work. The outflows reported in this thesis however, extend much further in both the molecular and ionised gas phase. The estimated molecular outflow mass is also reported to be larger than the mass reported by others studying this source.

To my knowledge, there are no other studies on ULIRGs that perform a spatially resolved analysis of outflow velocities. Cicone et al. (2018) applied a similar method to the study of galaxy NGC6240, but limited their spatially revolved analysis to molecular gas tracers (e.g. CO(1-0), CO(2-1) and CI(1-0) lines). The work presented here covers the outflow velocities of both the molecular and ionised gas phases, but limits itself to study the outflow mass rates of the molecular gas phase. For future work building on the methods described in this thesis, it would be interesting to see a comparative analysis of the outflow mass rates as a function of distance for the molecular, ionized and neutral gas phases. SFRs are often studied in relation to feedback. Following up on the possible stellar feedback driven molecular outflows, a spatially resolved analysis of the SFR in combination with the velocities and outflow mass rates for multiple gas phases for IRAS 20100 -4156 is recommended.

As demonstrated, studying one source in great detail can reveal interesting and useful knowledge about the complexity of feedback mechanisms in galaxies. However, studying samples of ULIRGs and the spatially resolved statistical relation between observables like SFR, outflow velocity and outflow mass rates including multiple gas phases, can give new detailed insight into the affects feedback has on SFR as a function of distance to the central AGN and the evolution of galaxies. I therefore recommend building on the methods described in this thesis for analysing spatially resolved outflows to include more sources and multiple gas phases.

Appendix

Additional plots

The Appendix reports additional plots relevant to the spectral line fitting of the CO and [OIII] line spectra. In particular, I show the plots comparing the fits performed using 2 or 3 Gaussian components.

CO(1-0) line

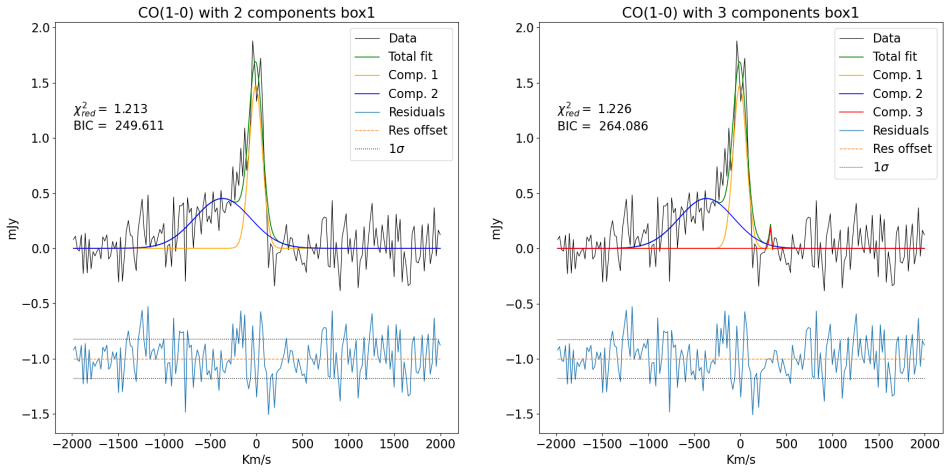

Figure 1: Plots comparing the fitting of two and three Gaussian components to the CO(1-0) line for box region 1. The observed continuum subtracted flux density is plotted in black in all panels. The total fit, which is the sum of all components is plotted in green. The fit residuals are plotted in blue, offset around the orange line and with $\pm\sigma$ levels in dashed lines. The χ^2_{red} and BIC is reported in each panel.

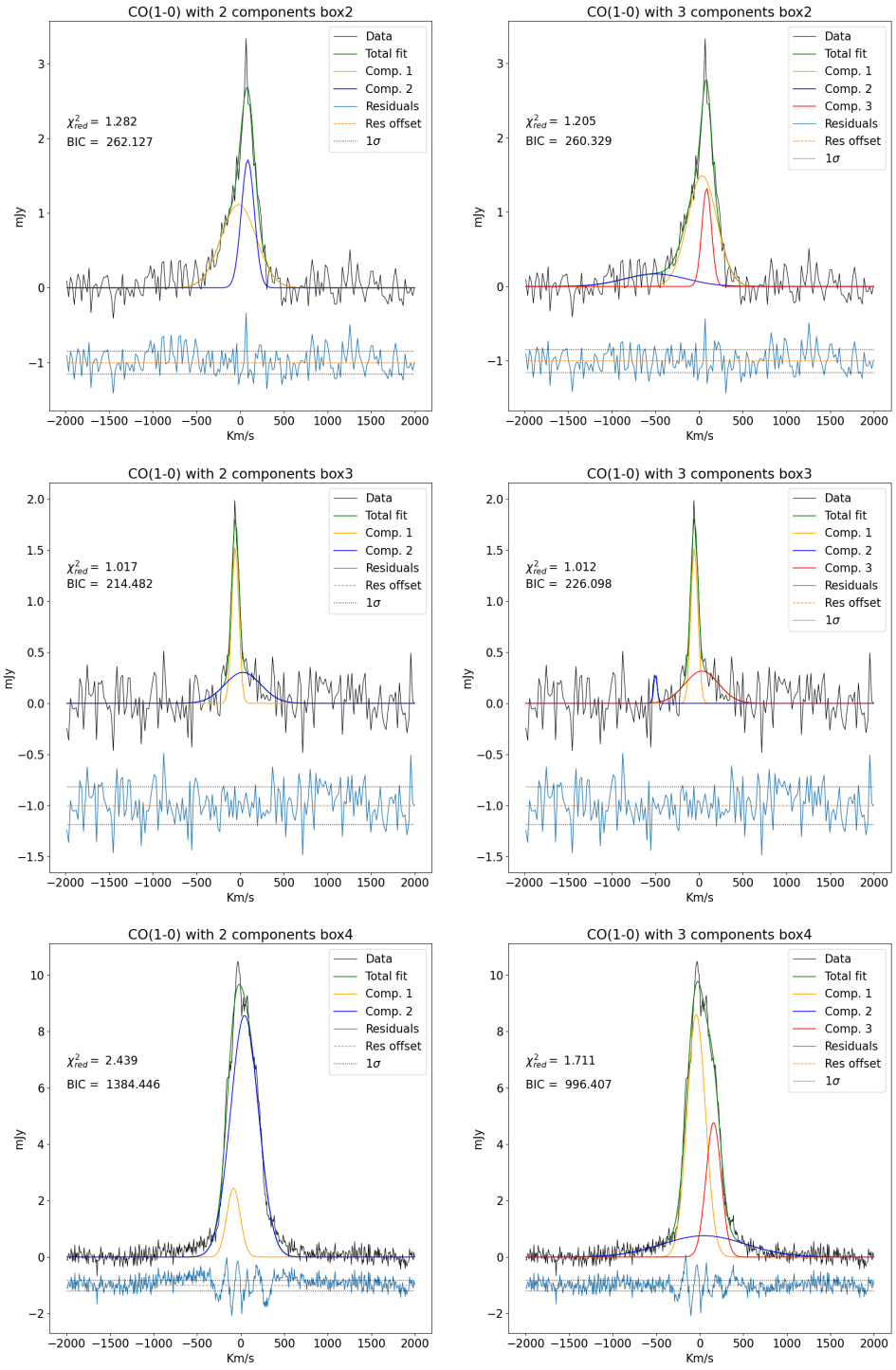

Figure 2: Plots comparing the fitting of two and three Gaussian components to the CO(1-0) line for box regions 2-4. The observed continuum subtracted flux density is plotted in black in all panels. The total fit, which is the sum of all components is plotted in green. The fit residuals are plotted in blue, offset around the orange line and with $\pm\sigma$ levels in dashed lines. The χ^2_{red} and BIC is reported in each panel.

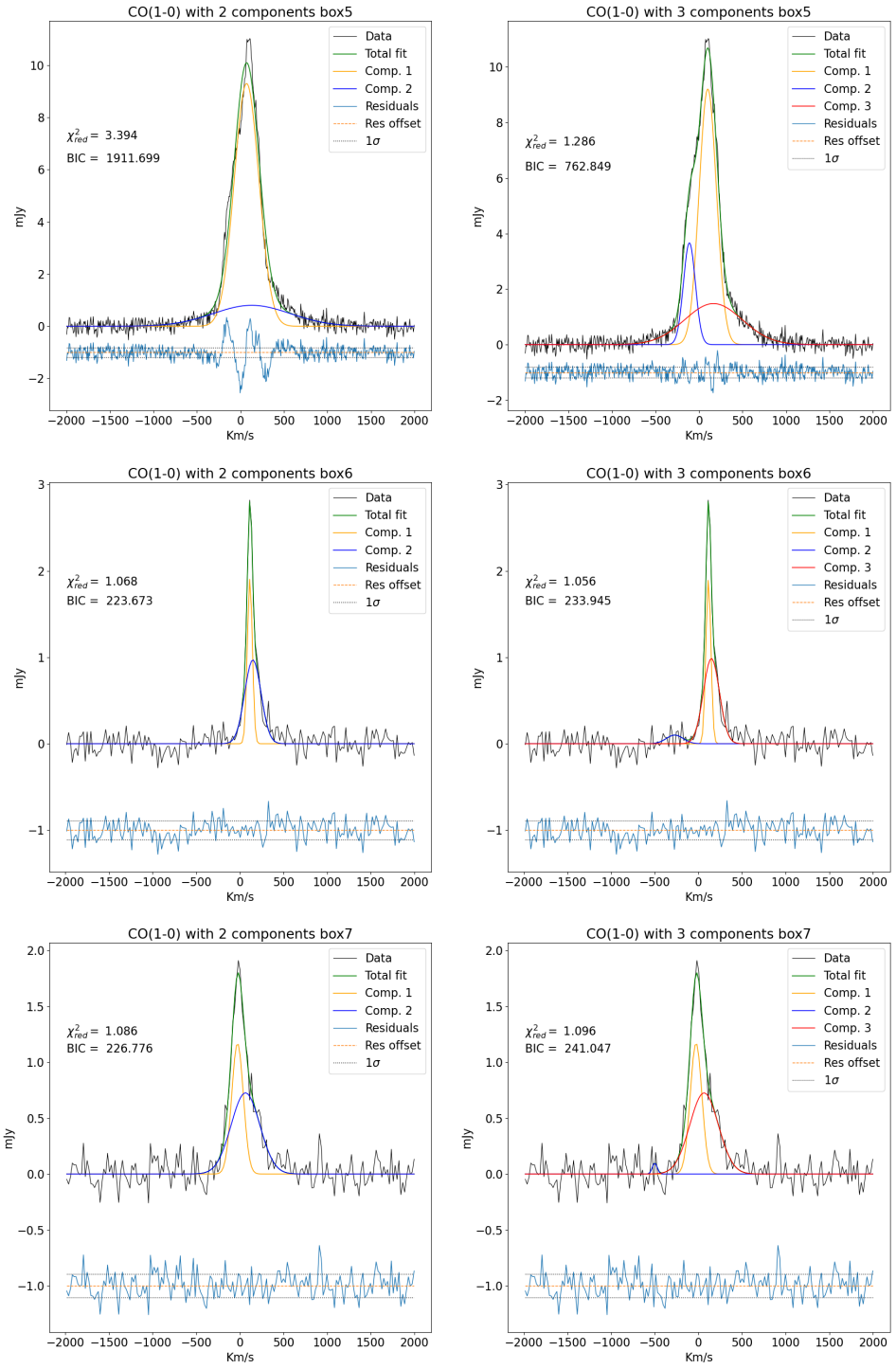

Figure 3: Plots comparing the fitting of two and three Gaussian components to the CO(1-0) line for box regions 5-7. The observed continuum subtracted flux density is plotted in black in all panels. The total fit, which is the sum of all components is plotted in green. The fit residuals are plotted in blue, offset around the orange line and with $\pm\sigma$ levels in dashed lines. The χ^2_{red} and BIC is reported in each panel.

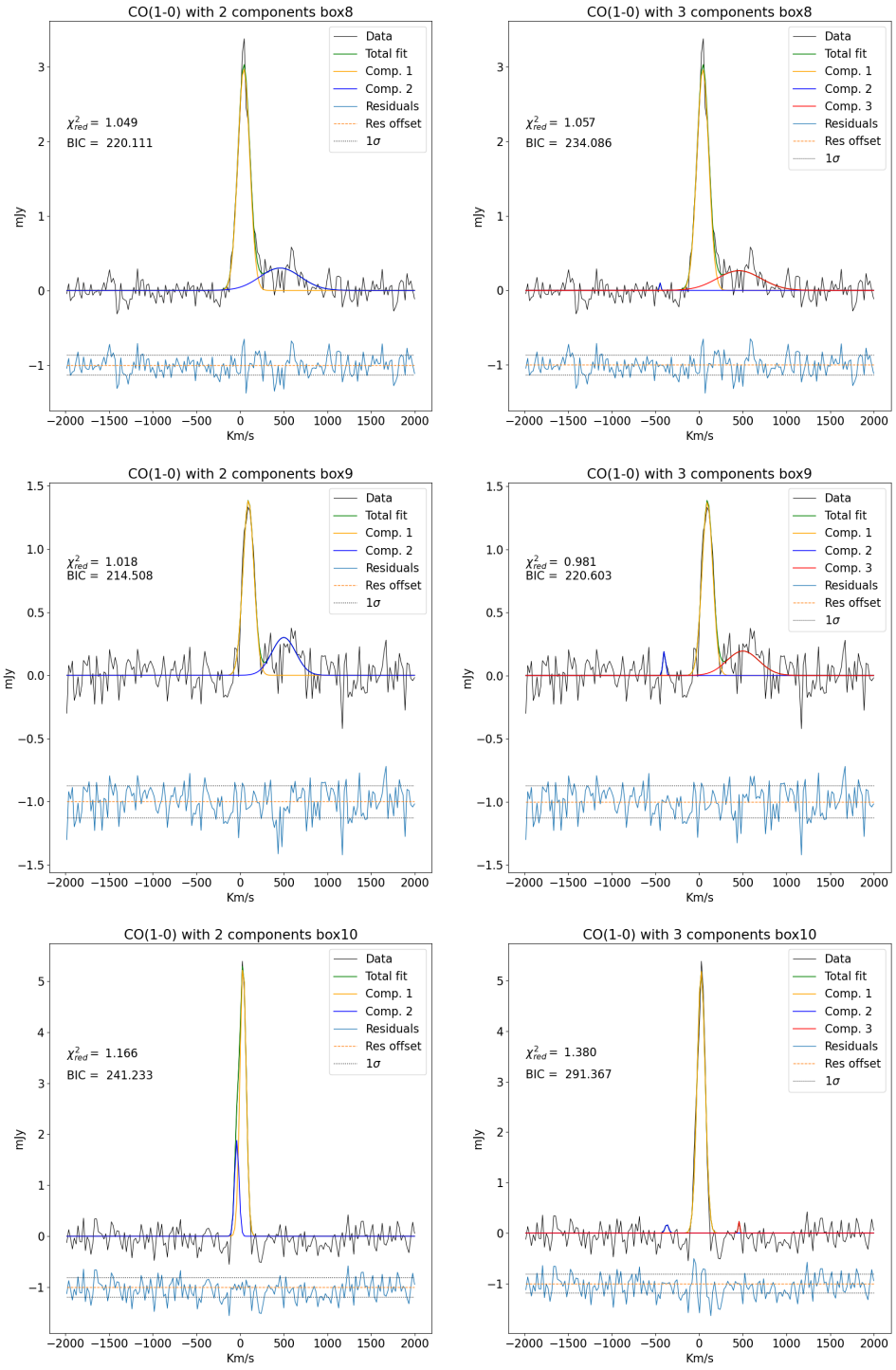

Figure 4: Plots comparing the fitting of two and three Gaussian components to the CO(1-0) line for box regions 8-10. The observed continuum subtracted flux density is plotted in black in all panels. The total fit, which is the sum of all components is plotted in green. The fit residuals are plotted in blue, offset around the orange line and with $\pm\sigma$ levels in dashed lines. The χ^2_{red} and BIC is reported in each panel.

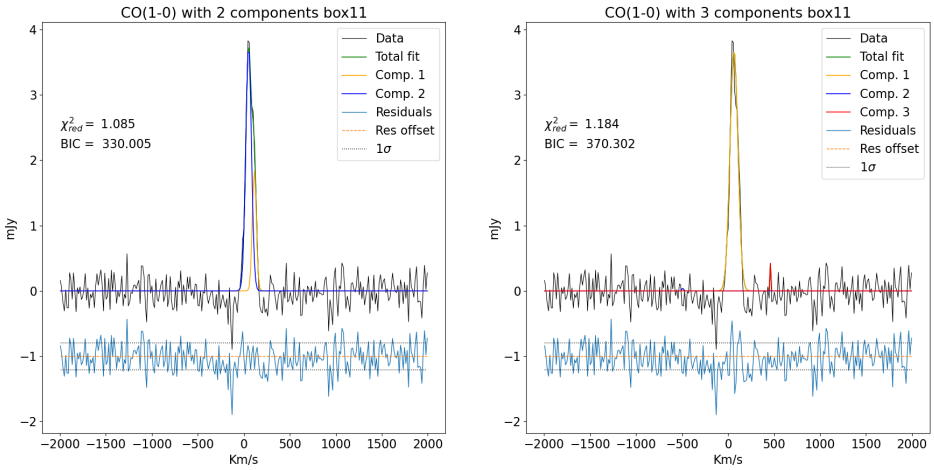

Figure 5: Plots comparing the fitting of two and three Gaussian components to the CO(1-0) line for box region 11. The observed continuum subtracted flux density is plotted in black in all panels. The total fit, which is the sum of all components is plotted in green. The fit residuals are plotted in blue, offset around the orange line and with $\pm\sigma$ levels in dashed lines. The χ^2_{red} and BIC is reported in each panel.

[OIII] line

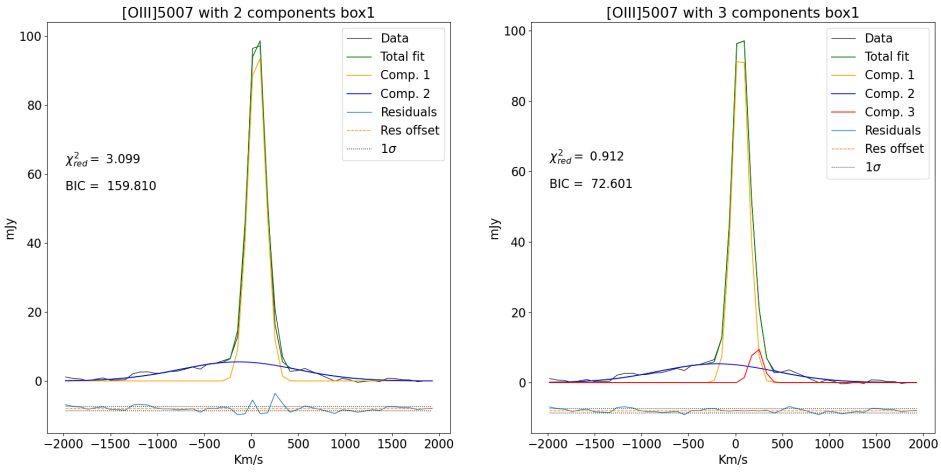

Figure 6: Plots comparing the fitting of two and three Gaussian components to the [OIII] line for box region 1. The observed continuum subtracted flux density is plotted in black in all panels. The total fit, which is the sum of all components is plotted in green. The fit residuals are plotted in blue, offset around the orange line and with $\pm\sigma$ levels in dashed lines. The χ^2_{red} and BIC is reported in each panel.

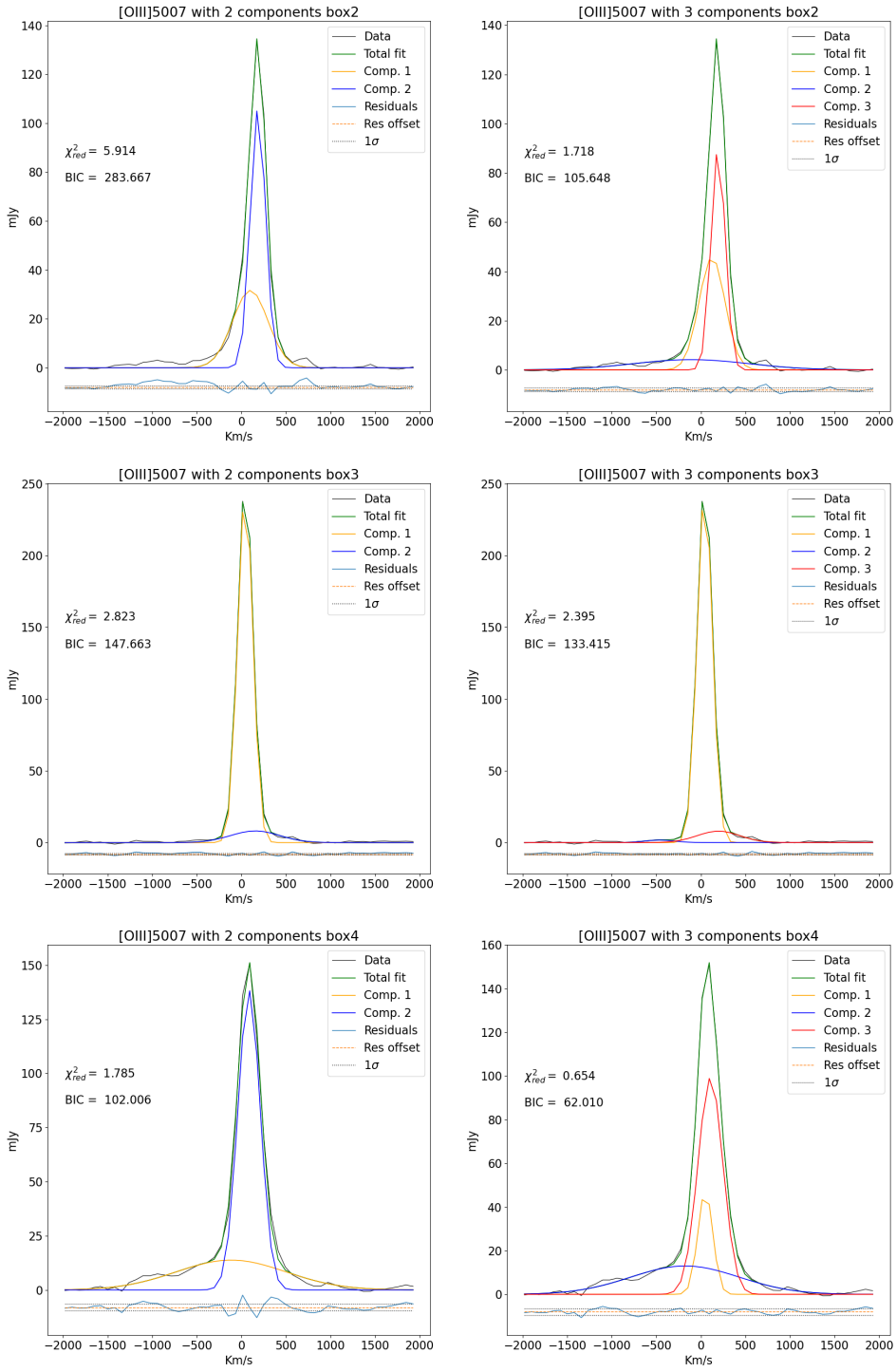

Figure 7: Plots comparing the fitting of two and three Gaussian components to the [OIII] line for box regions 2-4. The observed continuum subtracted flux density is plotted in black in all panels. The total fit, which is the sum of all components is plotted in green. The fit residuals are plotted in blue, offset around the orange line and with $\pm\sigma$ levels in dashed lines. The χ^2_{red} and BIC is reported in each panel.

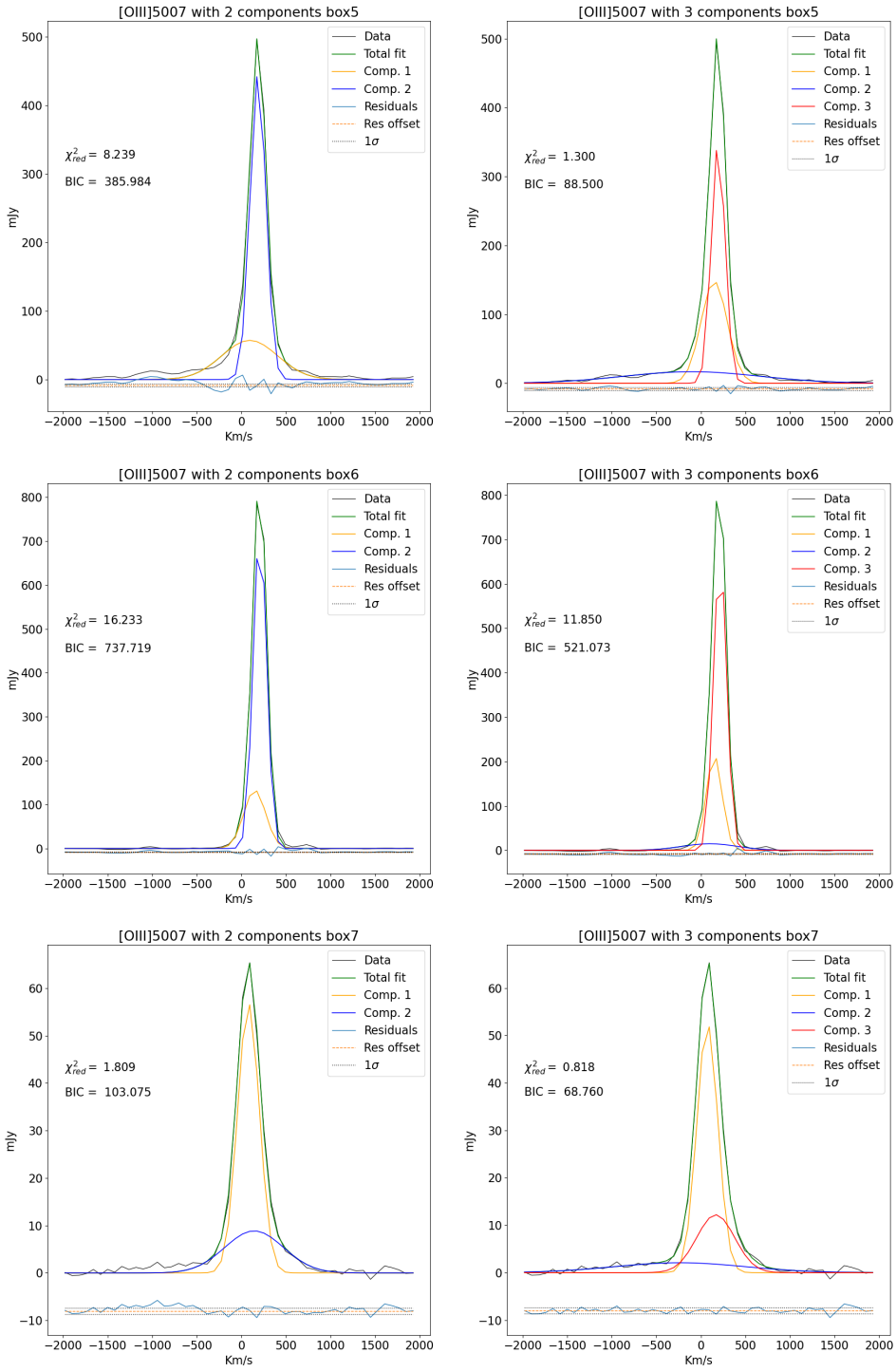

Figure 8: Plots comparing the fitting of two and three Gaussian components to the [OIII] line for box regions 5-7. The observed continuum subtracted flux density is plotted in black in all panels. The total fit, which is the sum of all components is plotted in green. The fit residuals are plotted in blue, offset around the orange line and with $\pm\sigma$ levels in dashed lines. The χ^2_{red} and BIC is reported in each panel.

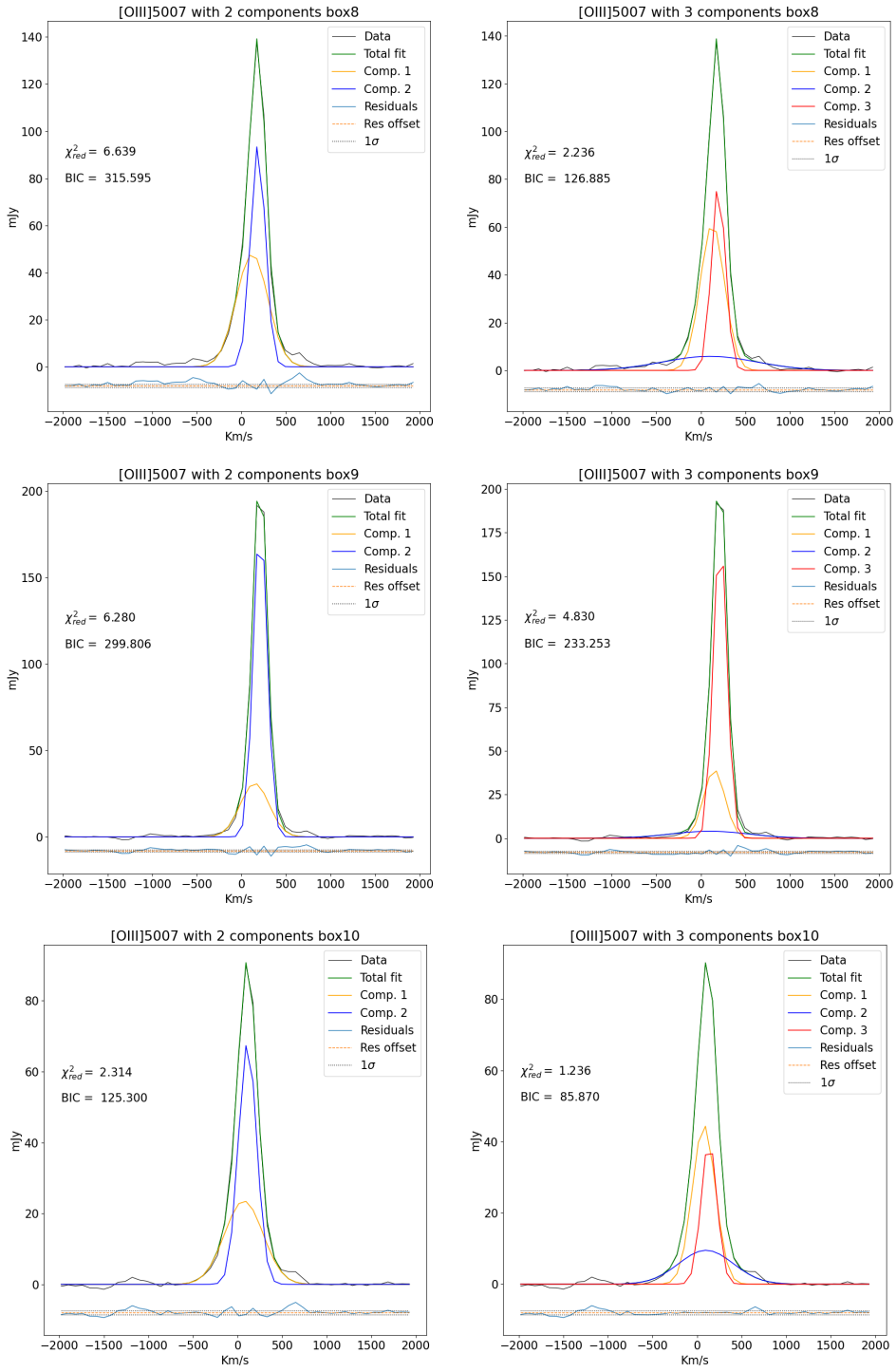

Figure 9: Plots comparing the fitting of two and three Gaussian components to the [OIII] line for box regions 8-10. The observed continuum subtracted flux density is plotted in black in all panels. The total fit, which is the sum of all components is plotted in green. The fit residuals are plotted in blue, offset around the orange line and with $\pm\sigma$ levels in dashed lines. The χ^2_{red} and BIC is reported in each panel.

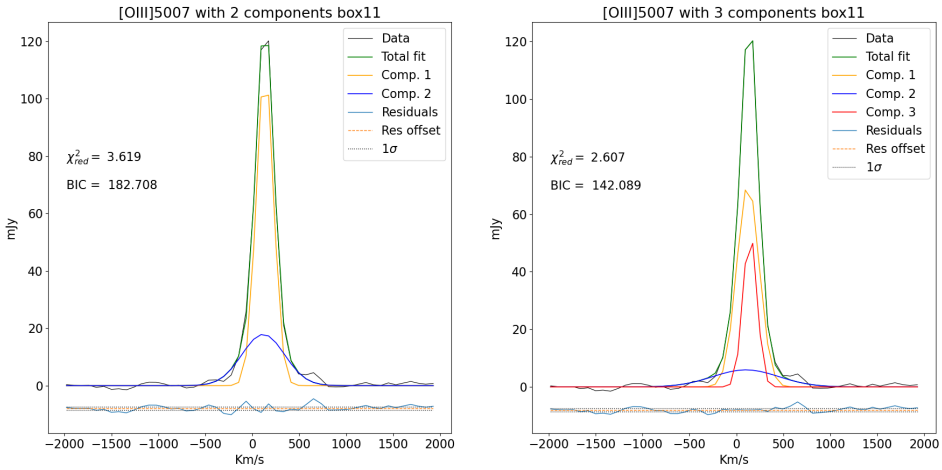

Figure 10: Plots comparing the fitting of two and three Gaussian components to the [OIII] line for box region 11. The observed continuum subtracted flux density is plotted in black in all panels. The total fit, which is the sum of all components is plotted in green. The fit residuals are plotted in blue, offset around the orange line and with $\pm\sigma$ levels in dashed lines. The χ^2_{red} and BIC is reported in each panel.

Bibliography

Barger, A. J., Cowie, L. L., Sanders, D. B., Fulton, E., Taniguchi, Y., Sato, Y., Kawara, K., and Okuda, H. (1998). Submillimetre-wavelength detection of dusty star-forming galaxies at high redshift. *Nature*, 394:248–251. ADS Bibcode: 1998Natur.394..248B.

Beckmann, V. and Shrader, C. (2012a). The AGN phenomenon: open issues. page 69. Conference Name: Proceedings of "An INTEGRAL view of the high-energy sky (the first 10 years)" - 9th INTEGRAL Workshop and celebration of the 10th anniversary of the launch (INTEGRAL 2012). 15-19 October 2012. Bibliotheque Nationale de France Place: eprint: arXiv:1302.1397 ADS Bibcode: 2012int..workE..69B.

Beckmann, V. and Shrader, C. R. (2012b). *Active Galactic Nuclei*. Publication Title: Active Galactic Nuclei ADS Bibcode: 2012agn..book.....B.

Cappellari, M. (2017). Improving the full spectrum fitting method: accurate convolution with Gauss-Hermite functions. *Monthly Notices of the Royal Astronomical Society*, 466:798–811. ADS Bibcode: 2017MNRAS.466..798C.

Cappellari, M. and Emsellem, E. (2004). Parametric Recovery of Line-of-Sight Velocity Distributions from Absorption-Line Spectra of Galaxies via Penalized Likelihood. *Publications of the Astronomical Society of the Pacific*, 116:138–147. ADS Bibcode: 2004PASP..116..138C.

Cazzoli, S. (2017). Negative and positive outflow-feedback in nearby (U)LIRGs. *Frontiers in Astronomy and Space Sciences*, 4:62. ADS Bibcode: 2017FrASS...4...62C.

Cicone, C., Severgnini, P., Papadopoulos, P. P., Maiolino, R., Feruglio, C., Treister, E., Privon, G. C., Zhang, Z.-y., Della Ceca, R., Fiore, F., Schawinski, K., and Wagg, J. (2018). ALMA [C I]3 P 1-3 P 0 Observations of NGC 6240: A Puzzling Molecular Outflow, and the Role of Outflows in the Global Î±$COFactorof(U)LIRGs$. $TheAstrophysicalJournal$, 863 : 143. $ADSBibcode$: 2018ApJ...863..143C.

Daddi, E., Dickinson, M., Chary, R., Pope, A., Morrison, G., Alexander, D. M., Bauer, F. E., Brandt, W. N., Giavalisco, M., Ferguson, H., Lee, K. S., Lehmer, B. D., Papovich, C., and Renzini, A. (2005). The Population of BzK-selected ULIRGs at z ~ 2. *The Astrophysical Journal*, 631:L13–L16. ADS Bibcode: 2005ApJ...631L..13D.

Daddi, E., Elbaz, D., Walter, F., Bournaud, F., Salmi, F., Carilli, C., Dannerbauer, H., Dickinson, M., Monaco, P., and Riechers, D. (2010). Different Star Formation Laws for Disks Versus Starbursts at Low and High Redshifts. *The Astrophysical Journal*, 714:L118–L122. ADS Bibcode: 2010ApJ...714L.118D.

Draper, P. W., Gray, N., Berry, D. S., and Taylor, M. (2014). GAIA: Graphical Astronomy and Image Analysis Tool. *Astrophysics Source Code Library*, page ascl:1403.024. ADS Bibcode: 2014ascl.soft03024D.

Duc, P.-A., Mirabel, I. F., and Maza, J. (1997). Southern ultraluminous infrared galaxies: an optical and infrared database. *A & A Supplement series, Vol. 124, September 1997, p.533-557.*, 124:533.

Ellison, S. L., Mendel, J. T., Patton, D. R., and Scudder, J. M. (2013). Galaxy pairs in the Sloan Digital Sky Survey - VIII. The observational properties of post-merger galaxies. *Monthly Notices of the Royal Astronomical Society*, 435:3627–3638. ADS Bibcode: 2013MNRAS.435.3627E.

Fabian, A. C. (1999). Active Galactic Nuclei. *Proceedings of the National Academy of Science*, 96:4749–4751. ADS Bibcode: 1999PNAS...96.4749F.

Ferrarese, L. and Ford, H. (2005). Supermassive Black Holes in Galactic Nuclei: Past, Present and Future Research. *Space Science Reviews*, 116:523–624. ADS Bibcode: 2005SSRv..116..523F.

Fluetsch, A., Maiolino, R., Carniani, S., Arribas, S., Belfiore, F., Bellocchi, E., Cazzoli, S., Cicone, C., Cresci, G., Fabian, A. C., Gallagher, R., Ishibashi, W., Mannucci, F., Marconi, A., Perna, M., Sturm, E., and Venturi, G. (2021). Properties of the multiphase outflows in local (ultra)luminous infrared galaxies. *Monthly Notices of the Royal Astronomical Society*, 505:5753–5783. ADS Bibcode: 2021MNRAS.505.5753F.

Fluetsch, A., Maiolino, R., Carniani, S., Marconi, A., Cicone, C., Bourne, M. A., Costa, T., Fabian, A. C., Ishibashi, W., and Venturi, G. (2019). Cold molecular outflows in the local Universe and their feedback effect on galaxies. *Monthly Notices of the Royal Astronomical Society*, 483:4586–4614. ADS Bibcode: 2019MNRAS.483.4586F.

Genzel, R., Tacconi, L. J., Gracia-Carpio, J., Sternberg, A., Cooper, M. C., Shapiro, K., Bolatto, A., BouchÃ©, N., Bournaud, F., Burkert, A., Combes, F., Comerford, J., Cox, P., Davis, M., FÃ¶rster Schreiber, N. M., Garcia-Burillo, S., Lutz, D., Naab, T., Neri, R., Omont, A., Shapley, A., and Weiner, B. (2010). A study of the gas-star formation relation over cosmic time. *Monthly Notices of the Royal Astronomical Society*, 407:2091–2108. ADS Bibcode: 2010MNRAS.407.2091G.

Gowardhan, A., Spoon, H., Riechers, D. A., GonzÃ¡lez-Alfonso, E., Farrah, D., Fischer, J., Darling, J., Fergulio, C., Afonso, J., and Bizzocchi, L. (2018). The Dual Role of Starbursts and Active Galactic Nuclei in Driving Extreme Molecular Outflows. *The Astrophysical Journal*, 859:35. ADS Bibcode: 2018ApJ...859...35G.

Gruppioni, C., Pozzi, F., Rodighiero, G., Delvecchio, I., Berta, S., Pozzetti, L., Zamorani, G., Andreani, P., Cimatti, A., Ilbert, O., Le Floc'h, E., Lutz, D., Magnelli, B., Marchetti, L., Monaco, P., Nordon, R., Oliver, S., Popesso, P., Riguccini, L., Roseboom, I., Rosario, D. J., Sargent, M., Vaccari, M., Altieri, B., Aussel, H., Bongiovanni, A., Cepa, J., Daddi, E., DomÃnguez-SÃ¡nchez, H., Elbaz, D., Forster Schreiber, N., Genzel, R., Iribarrem, A., Magliocchetti, M., Maiolino, R., Poglitsch, A., PÃ©rez GarcÃa, A., Sanchez-Portal, M., Sturm, E., Tacconi, L., Valtchanov, I., Amblard, A., Arumugam, V., Bethermin, M., Bock, J., Boselli, A., Buat, V., Burgarella, D., Castro-RodrÃguez, N., Cava, A., Chanial, P., Clements, D. L., Conley, A., Cooray, A., Dowell, C. D., Dwek, E., Eales, S., Franceschini, A., Glenn, J., Griffin, M., Hatziminaoglou, E., Ibar, E., Isaak, K., Ivison, R. J., Lagache, G., Levenson, L., Lu, N., Madden, S., Maffei, B., Mainetti, G., Nguyen, H. T., O'Halloran, B., Page, M. J., Panuzzo, P., Papageorgiou, A., Pearson, C. P., PÃ©rez-Fournon, I., Pohlen, M., Rigopoulou, D., Rowan-Robinson, M., Schulz, B., Scott, D., Seymour, N., Shupe, D. L., Smith, A. J., Stevens, J. A., Symeonidis, M., Trichas, M., Tugwell, K. E., Vigroux, L., Wang, L., Wright, G., Xu, C. K., Zemcov, M., Bardelli, S., Carollo, M., Contini, T., Le FÃ©vre, O., Lilly, S., Mainieri, V., Renzini, A., Scodeggio, M., and Zucca, E. (2013). The Herschel PEP/HerMES luminosity function - I. Probing the evolution of PACS selected Galaxies to z â 4. *Monthly Notices of the Royal Astronomical Society*, 432:23–52. ADS Bibcode: 2013MNRAS.432...23G.

Hogbom, J. A. (2003). Early Work in Imaging. 300:17. Conference Name: Radio Astronomy at the Fringe ADS Bibcode: 2003ASPC..300...17H.

Hopkins, P. F., Hernquist, L., Cox, T. J., Di Matteo, T., Robertson, B., and Springel, V. (2006). A Unified, Merger-driven Model of the Origin of Starbursts, Quasars, the Cosmic X-Ray Background, Supermassive Black Holes, and Galaxy Spheroids. *The Astrophysical Journal Supplement Series*, 163:1–49. ADS Bibcode: 2006ApJS..163....1H.

Joseph, R. D. and Wright, G. S. (1985). Recent star formation in interacting galaxies - II. Super starbursts in merging galaxies. *Monthly Notices of the Royal Astronomical Society*, 214:87–95. ADS Bibcode: 1985MNRAS.214...87J.

Knapen, J. H., Cisternas, M., and Querejeta, M. (2015). Interacting galaxies in the nearby Universe: only moderate increase of star formation. *Monthly Notices of the Royal Astronomical Society*, 454:1742–1750. ADS Bibcode: 2015MNRAS.454.1742K.

Lin, L., Patton, D. R., Koo, D. C., Casteels, K., Conselice, C. J., Faber, S. M., Lotz, J., Willmer, C. N. A., Hsieh, B. C., Chiueh, T., Newman, J. A., Novak, G. S., Weiner, B. J., and Cooper, M. C. (2008). The Redshift Evolution of Wet, Dry, and Mixed Galaxy Mergers from Close Galaxy Pairs in the DEEP2 Galaxy Redshift Survey. *The Astrophysical Journal*, 681:232–243. ADS Bibcode: 2008ApJ...681..232L.

Madau, P. and Dickinson, M. (2014). Cosmic Star-Formation History. *Annual Review of Astronomy and Astrophysics, vol. 52, p.415-486*, 52:415.

McMullin, J. P., Waters, B., Schiebel, D., Young, W., and Golap, K. (2007). CASA Architecture and Applications. 376:127. Conference Name: Astronomical Data Analysis Software and Systems XVI ADS Bibcode: 2007ASPC..376..127M.

Murase, T., Handa, T., Hirata, Y., Omodaka, T., Nakano, M., Sunada, K., Shimajiri, Y., and Nishi, J. (2022). Kagoshima galactic object survey with the Nobeyama 45-metre telescope by mapping in ammonia lines (KAGONMA): star formation feedback on dense molecular gas in the W33 complex. *Monthly Notices of the Royal Astronomical Society*, 510:1106–1117. ADS Bibcode: 2022MNRAS.510.1106M.

Naab, T., Khochfar, S., and Burkert, A. (2006). Properties of Early-Type, Dry Galaxy Mergers and the Origin of Massive Elliptical Galaxies. *The Astrophysical Journal*, 636:L81–L84. ADS Bibcode: 2006ApJ...636L..81N.

Netzer, H. (2015). Revisiting the Unified Model of Active Galactic Nuclei. *Annual Review of Astronomy and Astrophysics, vol. 53, p.365-408*, 53:365.

Pearson, W. J., Wang, L., Alpaslan, M., Baldry, I., Bilicki, M., Brown, M. J. I., Grootes, M. W., Holwerda, B. W., Kitching, T. D., Kruk, S., and van der Tak, F. F. S. (2019). Effect of galaxy mergers on star-formation rates. *Astronomy & Astrophysics, Volume 631, id.A51,19*, 631:A51.

Perez, J., Michel-Dansac, L., and Tissera, P. B. (2011). Chemical evolution during gas-rich galaxy interactions. *Monthly Notices of the Royal Astronomical Society*, 417:580–590. ADS Bibcode: 2011MNRAS.417..580P.

Perna, M., Arribas, S., Pereira Santaella, M., Colina, L., Bellocchi, E., Catalan-Torrecilla, C., Cazzoli, S., Crespo Gomez, A., Maiolino, R., Piqueras Lopez, J., and Rodriguez del Pino, B. (2021). Physics of ULIRGs with MUSE and ALMA: The PUMA project. I. Properties of the survey and first MUSE data results. *Astronomy & Astrophysics, Volume 646, id.A101, 58.*, 646:A101.

Putman, M. E. (2017). An Introduction to Gas Accretion onto Galaxies. 430:1. Conference Name: Gas Accretion onto Galaxies Place: eprint: arXiv:1612.00461 ADS Bibcode: 2017ASSL..430....1P.

Schweizer, F. (2005). Merger-Induced Starbursts. 329:143. Conference Name: Starbursts: From 30 Doradus to Lyman Break Galaxies Place: eprint: arXiv:astro-ph/0502111 ADS Bibcode: 2005ASSL..329..143S.

Silva, A., Marchesini, D., Silverman, J. D., Skelton, R., Iono, D., Martis, N., Marsan, Z. C., Tadaki, K.-i., Brammer, G., and kartaltepe, J. (2018). Galaxy Mergers up to $Z < 2.5$. I. The Star Formation Properties of Merging Galaxies at Separations of 3-15 kpc. *The Astrophysical Journal*, 868:46. ADS Bibcode: 2018ApJ...868...46S.

Solomon, P. M. and Vanden Bout, P. A. (2005). Molecular Gas at High Redshift. *Annual Review of Astronomy & Astrophysics, vol. 43, Issue 1, pp.677-725*, 43(1):677.

Tacconi, L. J., Neri, R., Genzel, R., Combes, F., Bolatto, A., Cooper, M. C., Wuyts, S., Bournaud, F., Burkert, A., Comerford, J., Cox, P., Davis, M., Forster Schreiber, N. M., GarcÃa-Burillo, S., Gracia-Carpio, J., Lutz, D., Naab, T., Newman, S., Omont, A., Saintonge, A., Shapiro Griffin, K., Shapley, A., Sternberg, A., and Weiner, B. (2013). Phibss: Molecular Gas Content and Scaling Relations in z ˜ 1-3 Massive, Main-sequence Star-forming Galaxies. *The Astrophysical Journal*, 768:74. ADS Bibcode: 2013ApJ...768...74T.

Urry, C. M. and Padovani, P. (1995). Unified Schemes for Radio-Loud Active Galactic Nuclei. *Publications of the Astronomical Society of the Pacific*, 107:803. ADS Bibcode: 1995PASP..107..803U.

Veilleux, S., Maiolino, R., Bolatto, A. D., and Aalto, S. (2020). Cool outflows in galaxies and their implications. *The Astronomy and Astrophysics Review, Volume 28, Issue 1, article id.2*, 28(1):2.

Veilleux, S., MelÃ©ndez, M., Sturm, E., Gracia-Carpio, J., Fischer, J., GonzÃ¡lez-Alfonso, E., Contursi, A., Lutz, D., Poglitsch, A., Davies, R., Genzel, R., Tacconi, L., de Jong, J. A., Sternberg, A., Netzer, H., Hailey-Dunsheath, S., Verma, A., Rupke, D. S. N., Maiolino, R., Teng, S. H., and Polisensky, E. (2013). Fast Molecular Outflows in Luminous Galaxy Mergers: Evidence for Quasar Feedback from Herschel. *The Astrophysical Journal*, 776:27. ADS Bibcode: 2013ApJ...776...27V.

Veilleux, S., Rupke, D. S. N., Kim, D. C., Genzel, R., Sturm, E., Lutz, D., Contursi, A., Schweitzer, M., Tacconi, L. J., Netzer, H., Sternberg, A., Mihos, J. C., Baker, A. J., Mazzarella, J. M., Lord, S., Sanders, D. B., Stockton, A., Joseph, R. D., and Barnes, J. E. (2009). Spitzer Quasar and Ulirg Evolution Study (QUEST). IV. Comparison of 1 Jy Ultraluminous Infrared Galaxies with Palomar-Green Quasars. *The Astrophysical Journal Supplement Series*, 182:628–666. ADS Bibcode: 2009ApJS..182..628V.

Whitaker, K. E., Franx, M., Leja, J., van Dokkum, P. G., Henry, A., Skelton, R. E., Fumagalli, M., Momcheva, I. G., Brammer, G. B., LabbÃ©, I., Nelson, E. J., and Rigby, J. R. (2014). Constraining the Low-mass Slope of the Star Formation Sequence at $0.5 < z < 2.5$. *The Astrophysical Journal*, 795:104. ADS Bibcode: 2014ApJ...795..104W.